Posted on 11 Feb 2026 — The copyright holder is the author/funder. All rights reserved. No reuse without permission. — https://doi.org/10.22541/essoar.177082653.32028814/v1 — This is a preprint and has not been peer-reviewed. Data may be preliminary.

The 2 May 2025 Mw 7.4 Drake Passage Earthquake: Insights into Tectonics at the Shackleton Fracture Zone-Chilean Trench Intersection

Alessandro Vuan[1], Giuseppe Brancatelli[2], Giuliano Brancolini[2], Luca Gasperini[3], Riccardo Geletti[1], Emanuele Lodolo[4], Andrea MAGRIN[5], Marco Menichetti[6], Milton Plasencia[7], Alina Polonia[8], Marco Santulin[2], and Alejandro Tassone[9]

[1]National Institute of Oceanography and Applied Geophysics - OGS
[2]Istituto Nazionale di Oceanografia e Geofisica Sperimentale
[3]Istituto di Scienze Marine, ISMAR, CNR
[4]Istituto Nazionale di Oceanografia e di Geofisica Sperimentale
[5]OGS
[6]University of Urbino
[7]Istituto Nazionale di Oceanografia e di Geofisica Sperimentale - OGS
[8]Institute of Marine Sciences, CNR
[9]University of Buenos Aires

February 11, 2026

Abstract

On 2 May 2025, a Mw 7.4 earthquake occurred ˜120 km off the southern tip of Tierra del Fuego, at the intersection of the Shackleton Fracture Zone and the Chilean Trench. This event is the largest recorded within this complex plate boundary, filling a gap between previous M>6 earthquakes. Most aftershocks exhibit compressional mechanisms with relatively steeply dipping planes, although some show strike-slip motion. To better resolve the activated fault system under limited station coverage, we relocated events and incorporated pP and pS phases identified using a trained classifier to constrain focal depths. Hypocentral depths range from 15 to 35 km, with the mainshock nucleating at 25 km. Aftershocks with predominantly reverse mechanisms cluster southeast of the mainshock along a steeply dipping structure near the Shackleton Fracture Zone. A 1997 multichannel seismic reflection profile crossing the epicentral region provides additional constraints on the possible complexity of the rupture process.

The 2 May 2025 Mw 7.4 Drake Passage Earthquake: Insights into Tectonics at the Shackleton Fracture Zone–Chilean Trench Intersection

A. Vuan[1], G. Brancatelli[1], G. Brancolini[1], L. Gasperini[2], R. Geletti[1], E. Lodolo[1], A. Magrin[1], M. Menichetti[3], M. Plasencia[1], A. Polonia[2], M. Santulin[1], A. Tassone[4]

[1]Istituto Nazionale di Oceanografia e di Geofisica Sperimentale - OGS, Italy
[2]Istituto di Scienze Marine - CNR-ISMAR, Bologna, Italy
[3]Dipartimento di Scienze Pure ed Applicate, Università di Urbino, Urbino, Italy
[4]Instituto de Geociencias Básicas, Aplicadas y Ambientales de Buenos Aires (IGeBA), CONICET - Universidad de Buenos Aires, Argentina

Key Points:

- 1. Largest instrumentally recorded quake at the intersection of the Shackleton Fracture Zone and the Chilean Trench.
- 2. Seismic data show the mainshock nucleated at ~25 km depth, within the downdip portion of the megathrust interface.
- 3. Relocated earthquakes indicate a complex rupture involving the Chilean megathrust and Shackleton Fracture Zone structures.

Corresponding author: Alessandro Vuan, avuan@ogs.it

Abstract

On 2 May 2025, a Mw 7.4 earthquake occurred ~120 km off the southern tip of Tierra del Fuego, at the intersection of the Shackleton Fracture Zone and the Chilean Trench. This event is the largest recorded within this complex plate boundary, filling a gap between previous M>6 earthquakes. Most aftershocks exhibit compressional mechanisms with relatively steeply dipping planes, although some show strike-slip motion. To better resolve the activated fault system under limited station coverage, we relocated events and incorporated pP and pS phases identified using a trained classifier to constrain focal depths. Hypocentral depths range from ~15 to 35 km, with the mainshock nucleating at ~25 km. Aftershocks with predominantly reverse mechanisms cluster southeast of the mainshock along a steeply dipping structure near the Shackleton Fracture Zone. A 1997 multichannel seismic reflection profile crossing the epicentral region provides additional constraints on the possible complexity of the rupture process.

Plain Language Summary

On 2 May 2025, a magnitude 7.4 earthquake struck about 120 km off the southern tip of South America near Tierra del Fuego. It was the strongest earthquake ever recorded in this complex region where several tectonic plates meet. The event ruptured a well-recognized seismic gap separating earlier earthquakes near the junction of major fault systems, none of which exceeded magnitude 6.5. Aftershocks mostly showed compressional motion on steeply dipping faults, which is unusual for a typical plate-boundary megathrust rupture, and a few showed strike-slip motion. Because seismic stations are sparse in this area, advanced methods were used to improve earthquake locations. By identifying depth-sensitive seismic phases with a machine-learning model, we determined that the mainshock began about 25 km deep, consistent with the very small tsunami observed. Aftershocks southeast of the epicenter occurred on westward-dipping faults near the Shackleton Fracture Zone. Older seismic imaging data also help illuminate the complex fault system involved.

1 Introduction

The Mw 7.4 earthquake of May 2, 2025, occurred off the southernmost tip of Tierra del Fuego (Fig. 1) and represents the strongest event ever documented in this region, where the southern terminus of the South American convergent plate boundary merges into the Shackleton Fracture Zone (SFZ). The event was initially interpreted as a reverse-faulting earthquake with a fixed depth of 10 km (United States Geological Survey, 2025), and aftershock distributions were described as indicating a rupture propagating southeastward along the SFZ. The reviewed focal mechanism (United States Geological Survey, 2025) shows a dominantly compressional source, a centroid depth of 23.5 km, and a NW–SE–striking nodal plane dipping either 33° to the northeast or 57° to the southwest, which is unusually steep for a shallow megathrust event along an active subduction zone (Bradley & Hubbard, 2025). In addition, the non–double-couple (NDC) component is anomalously high (37%), suggesting that sparse station coverage, an inadequate velocity model, and/or a complex source process may contribute to this elevated value.

A maximum slip of approximately 4-5 m has been estimated from finite-fault inversion (United States Geological Survey, 2025; Ji et al., 2002). However, this estimate is strongly influenced by the use of teleseismic stations located far from the epicentral region, resulting in significant uncertainty. For example, the centroid depth derived from the focal mechanism (23.5 km) is inconsistent with the shallow asperity inferred from the finite-fault model (United States Geological Survey, 2025). Given the complex structural configuration of this segment of the South American margin—where convergence along the Chilean Trench merges into left-lateral strike-slip deformation along the SFZ—it remains unclear whether the 2025 earthquake primarily reflects subduction-related pro-

cesses or complex reverse slip along the transform system. Transitions from subduction to strike-slip faulting along plate boundaries can arise from geometric segmentation, termination of the plate interface, block rotations, and/or changes in relative plate-motion trajectories (Wallace et al., 2012).

In this study, we analyze seismological data together with an unpublished multichannel seismic reflection profile crossing the epicentral area to constrain the 2025 seismic sequence and the shallow crustal architecture of the continental margin off Tierra del Fuego. Epicentral locations of the mainshock and its aftershocks are refined using seismic data from the regional ASAIN network (Vuan et al., 2014; Plasencia Linares et al., 2021), with a particular focus on constraining hypocentral depths. This is achieved through the application of trained models capable of identifying depth-sensitive seismic phases such as pP and pS. The 1997 multichannel seismic profile resolves the shallow architecture of the subduction system and offers important constraints on the location and geometry of the plate interface and major faults potentially involved in the 2025 rupture.

2 Geodynamic and tectonic setting

Structural development offshore southernmost Chile is driven by the relative movements between the Antarctica, Scotia, and South America plates. The boundary between the Scotia and South America plates is marked by the Magallanes–Fagnano fault system and the North Scotia Ridge (Lodolo et al., 2002, 2003), whereas the Antarctic–Scotia plate boundary follows the Chilean Trench to the northwest and the SFZ toward the southeast (Fig. 1). The triple junction between these plates (the Fuegian triple junction of Polonia et al. (2007) has been interpreted as a diffuse deformation zone located where the Magallanes–Fagnano fault system projects toward the Chilean Trench (Forsyth, 1975; Cunningham, 1993). North of this area, subduction involves the Antarctic and South America plates, whereas south of the triple junction, convergence between the Antarctic and Scotia plates becomes progressively more oblique and transitions into the transcurrent motion of the SFZ.

Post-Miocene convergence processes are characterized by subduction between the Antarctic and Scotia plates at a rate of ~10-20 mm yr^{-1} (DeMets et al., 1990). Seismic reflection profiles reveal strong variations in frontal-wedge morphology, accretion rates, and overall structural style. These variations occur along oblique structural trends that segment the margin, driven by processes on the overriding plate as well as by local heterogeneities on the incoming plate, such as seamounts, fracture zones, and oceanic fabric (Polonia et al., 2007).

The intra-oceanic SFZ is a northwest–southeast trending fracture zone extending over 800 km from the southernmost Chilean Trench to the eastern termination of the South Shetland Trench, where it subducts beneath the South Shetland Islands block (Aldaya & Maldonado, 1996; Klepeis & Lawver, 1996).

Seismicity and focal mechanisms indicate that the SFZ is an active, left-lateral transpressive fault zone that, together with the South Scotia Ridge, accommodates relative motion between the Scotia and Antarctic plates (Pelayo & Wiens, 1989; Barker et al., 1991; Livermore et al., 1994; Aldaya & Maldonado, 1996; Galindo-Zaldívar et al., 1996; Klepeis & Lawver, 1996; Maldonado et al., 2000). Bathymetric (British Antarctic Survey, 2012; Bohoyo et al., 2016) and seismic data further reveal that the SFZ exhibits pronounced relief, and is flanked to the east by a well-developed trough system (Geletti et al., 2005).

South of the Chile Triple Junction (Fig. 1), seismicity along the margin is low (Pelayo & Wiens, 1989), which may be partly attributed to slow convergence rates (5-10 mm/year, and the obliquity of convergence that promotes strain partitioning (Lodolo et al., 2003;

Geletti et al., 2005; Polonia et al., 2007; Civile et al., 2012). Despite the limited seismicity—insufficient to resolve the slab geometry from earthquake data alone—seismic reflection profiles indicate that the continental margin between 50°S and 56°S is characterized by large folds and active thrust faults (Polonia et al., 1999, 2007). These features suggest that margin-perpendicular shortening is still active, or has slowed only recently (Rubio et al., 2000).

Overall, this geodynamic and tectonic environment diverges markedly from that of a classic subduction margin. It remains unclear how, in southernmost South America, the Chilean megathrust interacts with the SFZ and associated splay faults to generate large-magnitude earthquakes.

3 Materials and Methods

Our analysis of the 2 May 2025 Drake Passage earthquake sequence integrates regional and teleseismic seismology with multichannel seismic reflection data. We first relocated the mainshock and aftershocks using high-quality P and S phases from the Antarctic Seismographic Argentinean Italian Network (ASAIN) (Plasencia Linares et al., 2021) and selected global stations (Fig. S1 and Tab. S1), applying the LocSAT (Bratt & Nagy, 1991) algorithm with the IASPEI91 velocity model (Kennett & Engdahl, 1991) (see Supplementary Text S1).

To better constrain hypocentral depths, we identified pP and sP depth phases using machine-learning tools from the SeisBench framework (Münchmeyer et al., 2023), enabling probabilistic multi-station depth estimation despite sparse regional coverage (see Supplementary Text S2 and Fig. S2). Focal mechanisms were compiled from multiple international agencies (Dziewonski et al., 1981; Ekström et al., 2012) to assess fault geometry and stress orientation.

We further reprocessed (see Supplementary Text S3) a 1997 multichannel seismic line (Polonia et al., 2007) crossing the epicentral region to image crustal structure and plate-boundary architecture relevant to the rupture (Fig. S3).

4 Results and interpretation

4.1 Relocated hypocenters and depth distribution

The mean residuals of the P phases at the most frequently used stations are shown in Figure S4, while Table S2 summarizes the P and S phases employed in the relocation, together with the average time residuals, epicentral distances, and azimuths for each station. Stations located closest to the events consistently display negative residuals, indicating that observed P arrivals occurred earlier than the theoretical predictions. The major axis of the epicentral uncertainty ellipses is oriented roughly east–west, reflecting the sparser station coverage in that direction (Fig. S5). Horizontal location uncertainties range from approximately 5 km in the latitudinal direction to 15–20 km in the longitudinal direction, with the lower resolution in longitude primarily due to limited coverage in the Scotia Sea and Pacific Ocean.

Figure 2 presents cross sections and map views of seismicity associated with the May 2, 2025 earthquake sequence, combining relocated hypocenters with pre-mainshock events listed in the ISC reviewed catalog (Bondár & Storchak, 2011). The relocated hypocenters (red) and earlier ISC catalog earthquakes (orange) are projected onto three vertical profiles designed to illustrate the geometry of seismicity in the region. Profile A–A′ is aligned with seismic reflection line IT97–245 and highlights the distribution of earthquakes across the continental margin. Profile B–B′ encompasses most aftershocks and illustrates the spatial extent and depth range of the post-mainshock sequence. Profile C–

C′ captures events intersecting the Shackleton Fracture Zone (SFZ), providing insight into how this major structural boundary influences faulting patterns.

Depth estimates are improved by incorporating depth phases such as pP and sP, although identifying these phases is often challenging in this region due to high noise levels. Figure 3 shows the likelihood distributions and depth estimates for each event obtained using the *DeepPhaseNet* and *DepthPhaseTEAM* trained models (Münchmeyer et al., 2023). Both approaches yield internally consistent depth determinations across the sequence. Figure S2 illustrates the stations providing pP and sP picks for each event, demonstrating the dense azimuthal coverage that supports stable depth estimation.

Aftershocks predominantly occur between ~15 and 35 km depth, defining a tightly constrained seismogenic zone that spans the lower crust and uppermost mantle. Only one shallow event (M 5.1) lies above this interval. Notably, the centroid depth reported by the USGS for the Mw 7.4 mainshock closely matches our model-based estimate, reinforcing both the robustness of the inferred depth distribution and the consistency between independent methodologies.

An assessment of the robustness of pP–P-derived depths is shown in Figure S6, where observed delay times (Δt) are compared with parametric sensitivity curves describing how inferred depth depends on (a) the assumed crustal P-wave velocity V_p, (b) the P-wave takeoff angle θ, and (c) the thickness L of a shallow low-velocity layer (LVL). Depths derived from focal mechanisms shown in Figure 2 are consistent with those estimated using depth phases.

4.2 Mainshock and aftershock mechanisms

Despite variations in centroid depth reported across different catalogs (Table S3), the dips of the possible fault planes in the GCMT and USGS solutions appear to be well constrained, as does the compressive orientation of the rupture. For the mainshock, both nodal planes indicate dips ranging from 33° to 52° (Fig. 2b), considerably steeper than the ∼5°–20° dip expected for the shallow Chilean megathrust. This suggests that the rupture likely occurred within one of the tectonic plates rather than along the plate interface, or that the rupture may be composite, involving multiple structures.

Analysis of historical focal mechanisms from the GCMT catalog since 1976 shows that dip angles in this region are consistently greater than 34° (Table S4). Similarly, Pelayo and Wiens (1989) reported two mb > 6.0 earthquakes in 1975 and 1976 with compressional mechanisms and dips exceeding 40°. Few early aftershocks exhibit strike-slip mechanisms with centroid depths of approximately 15 km (Table S5). Rose diagrams of P-axes (orientations ∼45°–60°, maximum compression) and T-axes (∼135°–150°, maximum tension) derived from these focal solutions are shown in the supplementary material (Fig. S7).

Taken together, these observations indicate a predominantly steeply dipping rupture. Nevertheless, given the compressional nature of the mainshock and its close proximity to the subduction interface, a contribution from the megathrust cannot be excluded, either in the form of direct slip or stress transfer to adjacent faults.

4.3 Seismic reflection profile and crustal structure

The time-migrated multichannel seismic line IT97–245 trends approximately orthogonal to the southernmost Chilean subduction system, extending from the oceanic trench to the continental shelf and passing near the epicenter of the May 2, 2025 earthquake (Figs. 1 and 2; profile A–A′). The Antarctic–Scotia plate boundary region is imaged to approximately 14 s two-way travel time (TWT). In the outer domain of the subduction system, the top of the Antarctic Plate oceanic basement dips landward, and the

oceanic crust is underlain at depth by the Moho reflector (Fig. 4a). The seafloor in the trench domain is relatively flat because the oceanic basement is buried beneath sediment infill at the trench axis. The accretionary wedge is about 20 km wide and is composed of deformed sediments scraped off the subducting Antarctic Plate and accreted along landward-dipping thrust faults that sole out against the main detachment.

Within the continental shelf, a well-developed sedimentary basin is clearly imaged (Fig. 4b). The basin depocenter contains a sedimentary section up to ∼2 s TWT thick. The location of this basin coincides with the northwestward continuation of the Shackleton Fracture Zone (SFZ), suggesting that the SFZ exerts a first-order control on the tectonic evolution of the region.

5 Discussion

The area where the Mw 7.4 earthquake occurred includes: (i) the southern end of the Andean subduction zone, where the interaction between the continental margin of Tierra del Fuego and the oceanic crust of the Antarctic Plate is highly oblique, and (ii) the northern termination of the left-lateral SFZ. Fault-plane solutions indicate a reverse mechanism for the May 2, 2025 mainshock, with a NE- or SW-dipping fault geometry. The nodal planes inferred near the trench ($\mathrm{dip}_1 > 35^\circ$ and $\mathrm{dip}_2 \approx 55$–$60^\circ$) are unusually steep for an Andean-type, shallow-dipping megathrust. Moreover, the temporal and spatial variation of dip angles (Fig. S8) reveals predominantly steep fault geometries, consistent with rupture along a relatively high-angle structure that may reflect the influence of oblique convergence and local tectonic segmentation.

Alternatively, such geometries may indicate: (1) a splay fault within the overriding plate that accommodates compressive stresses related to accretion; (2) rupture within a transition zone where the subducting slab begins to steepen; or (3) a composite source in which the mainshock triggered slip along one or more segments forming the northernmost part of the SFZ. Supporting evidence for a composite rupture is provided by morpho-bathymetric data (British Antarctic Survey, 2012; Bohoyo et al., 2016), which show that the SFZ bifurcates into at least two ridges to the north that parallel its main trace and extend onto the southern Tierra del Fuego continental shelf (Bohoyo et al., 2019). Similar morphologies occur along oceanic transverse ridges, such as those imaged across the Romanche and Vema fracture zones (Bonatti et al., 1994, 2005). The approximately east–west-directed stress regime in the Drake Passage region (Thomas et al., 2003) is largely dissipated along a narrow deformation zone within the SFZ, which is interpreted to result from crustal uplift and shortening (Geletti et al., 2005) and accommodates much of the present-day Antarctic–Scotia plate motion. Taken together, these observations support the activation of a composite source in which the megathrust interacts with the SFZ through transpressional and transtensional mechanisms, as also suggested by the distribution of aftershock seismicity.

The distribution of focal epicenters, which trend predominantly NW–SE, further supports this interpretation. The sedimentary basin imaged on the continental shelf in line IT97–245 (Fig. 4b) closely resembles other shelf basins along the western termination of the South America–Scotia plate boundary, where the Magallanes–Fagnano transform fault (Lodolo et al., 2003) intersects the southern Chilean Trench. In that region, a ∼3 km-thick sedimentary depocenter (the Madre de Dios Basin; (González, 1989)) develops (Polonia et al., 2007, their Fig. 6b), illustrating strong interaction between transform faulting and subduction processes.

The inversion of the mainshock focal mechanism in the USGS catalog reveals a 37% non–double-couple (NDC) component. Composite ruptures involving multiple fault types commonly generate large NDC values, which can range from negligible in simple settings to 20–48% in structurally complex environments (Tajima & Célérier, 1989; Frohlich &

Apperson, 1992; Ekström & Engdahl, 1989). Kuge and Kawakatsu (1992) showed that superposition of double-couple sources with rotating principal axes can produce significant NDC components. On a global scale, earthquakes with Mw > 6.5 in the GCMT catalog typically exhibit smaller NDC values (∼17%) (Rösler et al., 2021, 2023) than that inferred for the 2025 mainshock (37%), suggesting unresolved complexity in the source process.

The SFZ and related tectonic discontinuities within the incoming oceanic lithosphere can strongly perturb slab geometry and subduction processes along an active margin. Mechanical weakening along these discontinuities, combined with bending-related faulting, reduces effective strength and modifies slab buoyancy, promoting segmentation, tearing, and along-strike variations in subduction geometry. These processes influence interface coupling and stress transmission, resulting in spatially variable seismicity patterns and along-strike slab heterogeneity (Rodríguez et al., 2024). Based on these elements, we propose a kinematic scenario in which the mainshock nucleated between the obliquely subducting Antarctic Plate and the overriding Scotia Plate, within a highly heterogeneous crustal and upper-mantle structure. At subduction–transform transitions, the geometry of the plate interface may steepen abruptly over short distances or involve splay faults that appear steep in focal mechanisms. Composite sources involving contributions from megathrust patches, upper-plate reverse faults, and the SFZ can also produce steep nodal planes and large NDC values.

The event also generated transpressive stress at the intersection between the trench and the northern segment of the SFZ, where trench-normal and trench-parallel forces interact. This is the zone where oblique subduction transitions into strike-slip motion, and the convergence vector partitions into perpendicular and parallel components relative to the trench. In this complex structural scenario, portions of the overriding plate appear to be offset with respect to the SFZ trench-parallel strike, producing shallow faults that likely may move independently.

Similar transition zones occur along the New Zealand Hikurangi margin leading into the Alpine Fault system (Stevens et al., 2024), and in Sumatra where oblique convergence between the Indo-Australian and Eurasian plates is accommodated by the right-lateral Great Sumatran Fault (McNeill & Henstock, 2014; Moeremans et al., 2014).

6 Conclusions

Relocated hypocenters in the Drake Passage region indicate that seismogenic activity generally occurs between 15 km and approximately 35 km depth, consistent across both deep-learning–based approaches and traditional relocations using nearby regional stations. The May 2, 2025 mainshock nucleated at roughly 25 km depth.

Horizontal location uncertainties are larger in longitude due to sparse station coverage in the Scotia Sea, ranging from about 5 km to 20 km. Depth estimates constrained by pP and sP phases agree with depths reported for pre-2024 events in the ISC-reviewed bulletin located near the aftershock zone.

The depth distribution of seismicity, focal mechanism solutions, and structural constraints suggests that the mainshock originated in the interaction zone between a southwest-dipping structure associated with the SFZ and the Chilean megathrust. The predominantly compressional mechanisms with relatively steep dips, together with the clustering of aftershocks in the lower crust and upper mantle, support a composite rupture in which slip was partitioned across multiple fault segments.

Additional support comes from the multichannel seismic reflection profile, which clearly images the complex structural interaction between the shallow Chilean megathrust and the SFZ in the immediate vicinity of the Mw 7.4 hypocenter.

Open Research Section

All data used in this study are publicly available and properly cited in the references and supporting material.

Waveform and metadata used for event relocation and depth–phase analysis were obtained from the Antarctic Seismographic Argentinean Italian Network (ASAIN) and selected FDSN global stations (see Table S1 and Fig. S1 for station list and usage details). Data can be accessed at the EarthScope Data Center (IRIS DMC): `https://service.earthscope.org/fdsnws/dataselect/1/`, and at the ORFEUS Data Center (ORFEUS): `http://www.orfeus-eu.org/fdsnws/dataselect/1/`.

Regional catalog and focal–mechanism data prior to the mainshock were obtained from the International Seismological Centre (ISC) Reviewed Bulletin: `https://www.isc.ac.uk/iscbulletin/search/catalogue/`. Global Centroid Moment Tensor (GCMT) solutions were retrieved from `http://www.globalcmt.org`.

Source parameters and centroid solutions for the 2 May 2025 Drake Passage mainshock (Mw 7.4) were accessed from the USGS Earthquake Event Page: `https://earthquake.usgs.gov/earthquakes/eventpage/us7000pwkn` (accessed 21 January 2026).

Bathymetric grids used in Figures 1–2 derive from the General Bathymetric Chart of the Oceans (GEBCO): `https://www.gebco.net/data-products/gridded-bathymetry-data` (accessed 21 January 2026).

Seismic reflection data along line IT97–245 were reprocessed for this study; interpreted and uninterpreted seismic sections are provided as Figure 4 and Figure S3 in Supporting Information.

Software used for routine processing includes SeisComP (GFZ & Gempa GmbH, DOI: 10.5880/GFZ.2.4.2020.003). SeisComP relocation parameters are provided in Table S2 (Supporting Information). Depth–phase identification employed the SeisBench deep–learning models referenced in the manuscript and available at `https://zenodo.org/records/5568813`.

The derived relocated catalog is provided in QuakeML(https://quake.ethz.ch/quakeml) format as a supplementary file (events.qml).

All resources above are openly available or preserved in trusted repositories with persistent identifiers, in accordance with AGU policy requiring that data and code needed to understand, evaluate, and build upon the results be accessible at the time of review and publication.

Conflict of Interest declaration

The authors declare there are no conflicts of interest for this manuscript.

Acknowledgments

We thank the institutions and data providers that made this research possible. Seismic data were provided by the Antarctic Seismographic Argentinean Italian Network (ASAIN) and the International Seismological Centre (ISC). Bathymetric data were obtained from the British Antarctic Survey. We acknowledge the use of the SeisComP package (GFZ & Gempa GmbH, 2008). This work was supported by the Italian Programma Nazionale di Ricerche in Antartide (PNRA). We thank A. Camerlenghi for enabling the acquisition of the seismic line during the return from the Antarctic Peninsula, which took place over several days of fair weather, a rare condition at these latitudes. The authors acknowledge the scientific and logistic support of Dirección Nacional del Antártico (DNA) – In-

stituto Antártico Argentino (IAA) and the fundamental role of the Armada, Ejército, and Fuerza Aérea Argentina personnel in creating and maintaining the proper operating conditions for the ASAIN stations in the Antarctic bases.

References

Aldaya, F., & Maldonado, A. (1996). Tectonics of the triple junction at the southern end of the Shackleton Fracture Zone (Antarctic Peninsula). *Geo-Marine Letters*, *16*, 279–286. doi: 10.1007/BF01245558

Barker, P. F., Dalziel, I. W. D., & Storey, B. C. (1991). Tectonic development of the Scotia Arc region. In R. J. Tingey (Ed.), *The geology of antarctica* (pp. 215–248). Oxford: Clarendon Press.

Bohoyo, F., Larter, R. D., Galindo-Zaldívar, J., Leat, P. T., Maldonado, A., Tate, A. J., & Riley, T. R. (2019). Morphological and geological features of Drake Passage, Antarctica, from a new digital bathymetric model. *Journal of Maps*, *15*(2), 49–59. doi: 10.1080/17445647.2018.1543618

Bohoyo, F., Larter, R. D., Galindo-Zaldívar, J., Leat, P. T., Maldonado, A., Tate, A. J., ... Riley, T. R. (2016). *Bathymetry and geological setting of the Drake Passage* (BAS GEOMAP 2 Series). Cambridge: British Antarctic Survey.

Bonatti, E., Brunelli, D., Buck, W. R., Cipriani, A., Fabretti, P., Ferrante, V., ... Ligi, M. (2005). Flexural uplift of a lithospheric slab near the vema transform (Central Atlantic): Timing and mechanisms. *Earth and Planetary Science Letters*, *240*(3–4), 642–655. doi: 10.1016/j.epsl.2005.10.010

Bonatti, E., Ligi, M., Gasperini, L., Peyve, A., Raznitsin, Y., & Chen, Y. J. (1994). Transform migration and vertical tectonics at the Romanche fracture zone, equatorial Atlantic. *Journal of Geophysical Research: Solid Earth*, *99*(B11), 21779–21802. doi: 10.1029/94JB01178

Bondár, I., & Storchak, D. A. (2011). Improved location procedures at the international seismological centre. *Geophysical Journal International*, *186*, 1220–1244. doi: 10.1111/j.1365-246X.2011.05107.x

Bradley, K., & Hubbard, J. (2025). Unusual m7.4 earthquake strikes south of south america. *Earthquake Insights*. doi: 10.62481/0b850b61

Bratt, S. R., & Nagy, W. (1991). *The LocSAT Program* (Tech. Rep.). San Diego, CA: Science Applications International Corporation (SAIC). (User manual/report)

British Antarctic Survey. (2012). *High-resolution bathymetric data of the Shackleton Fracture Zone.* `https://www.bas.ac.uk/data/our-data/maps`. (Accessed Jan 21, 2026)

Civile, D., Lodolo, E., Vuan, A., & Loreto, M. F. (2012). Tectonics of the Scotia–Antarctica plate boundary constrained from seismic and seismological data. *Tectonophysics*, *550–553*, 17–34. doi: 10.1016/j.tecto.2012.05.002

Cunningham, W. D. (1993). Strike-slip faults in the southernmost Andes and the development of the Patagonian orocline. *Tectonics*, *12*(1), 169–186. doi: 10.1029/92TC01790

DeMets, C., Gordon, R. G., Argus, D. F., & Stein, S. (1990). Current plate motions. *Geophysical Journal International*, *101*, 425–478. doi: 10.1111/j.1365-246X.1990.tb06579.x

Dziewonski, A. M., Chou, T.-A., & Woodhouse, J. H. (1981). Determination of earthquake source parameters from waveform data for studies of global and regional seismicity. *Journal of Geophysical Research: Solid Earth*, *86*(B4), 2825–2852. doi: 10.1029/JB086iB04p02825

Ekström, G., & Engdahl, E. R. (1989). Earthquake source parameters and stress distribution in the Adak Island region of the central Aleutian Islands, Alaska. *Journal of Geophysical Research: Solid Earth*, *94*(B11), 15499–15519. doi: 10.1029/JB094iB11p15499

Ekström, G., Nettles, M., & Dziewonski, A. M. (2012). The global CMT project 2004–2010: Centroid-moment tensors for 13,017 earthquakes. *Physics of the Earth and Planetary Interiors*, *200–201*, 1–9. doi: 10.1016/j.pepi.2012.04.002

Forsyth, D. W. (1975). Fault plane solutions and tectonics of the South Atlantic and Scotia Sea. *Geophysical Journal International*, *80*, 1429–1443. doi: 10.1029/JB080i011p01429

Frohlich, C., & Apperson, K. D. (1992). Earthquake focal mechanisms, moment tensors, and the consistency of seismic activity near plate boundaries. *Tectonics*, *11*(2), 279–296. doi: 10.1029/91TC02888

Galindo-Zaldívar, J., Jabaloy, A., Maldonado, A., & Sanz de Galdeano, C. (1996). Continental fragmentation along the South Scotia Ridge transcurrent plate boundary (NE Antarctic Peninsula). *Tectonophysics*, *258*, 275–301. doi: 10.1016/0040-1951(95)00211-1

Geletti, R., Lodolo, E., Schreider, A. A., & Polonia, A. (2005). Seismic structure and tectonics of the Shackleton Fracture Zone (Drake Passage, Scotia Sea). *Marine Geophysical Research*, *26*, 17–28. doi: 10.1007/s11001-005-0147-4

GFZ, & Gempa GmbH. (2008). *The SeisComP seismological software package.* GFZ Data Services. doi: 10.5880/GFZ.2.4.2020.003

González, E. (1989). Hydrocarbon resources in the coastal zone of Chile. In G. E. Ericksen, M. T. Ganas Pinochet, & J. A. Reinemund (Eds.), *Geology of the andes and its relation to hydrocarbon and mineral resources* (Vol. 11, pp. 383–404). Houston, Texas: Circum-Pacific Council for Energy and Mineral Resources.

Ji, C., Wald, D. J., & Helmberger, D. V. (2002). Source description of the 1999 Hector Mine, California, earthquake. Part I: Wavelet domain inversion theory and resolution analysis. *Bulletin of the Seismological Society of America*, *92*(4), 1192–1207. doi: 10.1785/0120000916

Kennett, B. L. N., & Engdahl, E. R. (1991). Traveltimes for global earthquake location and phase identification. *Geophysical Journal International*, *105*(2), 429–465. doi: 10.1111/j.1365-246X.1991.tb06724.x

Klepeis, K. A., & Lawver, L. A. (1996). Tectonics of the Antarctic–Scotia plate boundary near Elephant and Clarence Islands, West Antarctica. *Journal of Geophysical Research: Solid Earth*, *101*(B9), 20211–20231. doi: 10.1029/96JB01510

Kuge, K., & Kawakatsu, H. (1992). Deep and intermediate-depth non-double-couple earthquakes: Interpretation of moment tensor inversions using various passbands of very broadband seismic data. *Geophysical Journal International*, *111*(3), 589–606. doi: 10.1111/j.1365-246X.1992.tb02114.x

Livermore, R., McAdoo, D., & Marks, K. (1994). Scotia Sea tectonics from high-resolution satellite gravity. *Earth and Planetary Science Letters*, *123*(1–3), 255–268. doi: 10.1016/0012-821X(94)90272-0

Lodolo, E., Menichetti, M., Bartole, R., Ben-Avraham, Z., Tassone, A., & Lippai, H. (2003). Magallanes–Fagnano continental transform fault (Tierra del Fuego, southernmost South America). *Tectonics*, *22*, 1076. doi: 10.1029/2003TC001500

Lodolo, E., Menichetti, M., Tassone, A., Geletti, R., Sterzai, P., Lippai, H., & Hormaechea, H.-L. (2002). Researchers target a continental transform fault in Tierra del Fuego. *Eos, Transactions American Geophysical Union*, *83*, 5–61. doi: 10.1029/2002EO000001

Maldonado, A., Carlos Balanyá, J., Barnolas, A., Galindo-Zaldívar, J., Hernández, J., Jabaloy, A., ... Viseras, C. (2000). Tectonics of an extinct ridge-transform intersection, Drake Passage (Antarctica). *Marine Geophysical Researches*, *21*, 43–68. doi: 10.1023/A:1004762311398

McNeill, L. C., & Henstock, T. J. (2014). Forearc structure and morphology along the Sumatra–Andaman subduction zone. *Tectonics*, *33*(2), 112–134. doi: 10

.1002/2012TC003264

Moeremans, R., Singh, S. C., Mukti, M., McArdle, J., & Johansen, K. (2014). Seismic images of structural variations along the deformation front of the Andaman–Sumatra subduction zone: Implications for rupture propagation and tsunamigenesis. *Earth and Planetary Science Letters*, *386*, 75–85. doi: 10.1016/j.epsl.2013.11.003

Münchmeyer, J., Saul, J., & Tilmann, F. (2023). Learning the Deep and the Shallow: Deep-Learning-Based Depth Phase Picking and Earthquake Depth Estimation. *Seismological Research Letters*, *95*(3), 1543–1557. doi: 10.1785/0220230187

Pelayo, A. M., & Wiens, D. A. (1989). Seismotectonics and relative plate motions in the Scotia Sea region. *Journal of Geophysical Research: Solid Earth*, *94*(B6), 7293–7320. doi: 10.1029/JB094iB06p07293

Plasencia Linares, M. P., Cravos, C., Laterza, R., Bernardi, P., Comelli, P., Grossi, M., ... Parolai, S. (2021). The Antarctic Seismographic Argentinean Italian Network (ASAIN): Recording Earthquakes in the Scotia Sea Region. *Seismological Research Letters*, *92*(5), 748–2757. doi: 10.1785/0220200484

Polonia, A., Brancolini, G., Torelli, L., & Vera, E. (1999). Structural variability at the active continental margin off southernmost Chile. *Journal of Geodynamics*, *27*, 289–307. doi: 10.1016/S0264-3707(98)00003-9

Polonia, A., Torelli, L., Brancolini, G., & Loreto, M.-F. (2007). Tectonic accretion versus erosion along the southern Chile trench: Oblique subduction and margin segmentation. *Tectonics*, *26*, TC3005. doi: 10.1029/2006TC001983

Rodríguez, E. E., Beck, S. L., Ruiz, M., Meltzer, A., Portner, D. E., Hernández, S., ... Charvis, P. (2024). Seismic imaging of the Northern Andean subduction zone from teleseismic tomography: A torn and fragmented Nazca slab. *Geophysical Journal International*, *236*, 593–606. doi: 10.1093/gji/ggad421

Rösler, B., Stein, S., & Spencer, B. D. (2021). Uncertainties in Seismic Moment Tensors Inferred from Differences Between Global Catalogs. *Seismological Research Letters*, *92*(6), 3698–3711. doi: 10.1785/0220210066

Rösler, B., Stein, S., & Spencer, B. D. (2023). When Are Non-Double-Couple Components of Seismic Moment Tensors Reliable? *Seismica*, *2*(1). doi: 10.26443/seismica.v2i1.241

Rubio, E., Torné, M., Vera, E., & Díaz, A. (2000). Crustal structure of the southernmost Chilean margin from seismic and gravity data. *Tectonophysics*, *323*(1–2), 39–60. doi: 10.1016/S0040-1951(00)00101-3

Stevens, D. E., McNeill, L. C., Henstock, T. J., Barnes, P. M., Crutchley, G., Bangs, N., ... Van Avendonk, H. J. A. (2024). Structural Variation Along the Southern Hikurangi Subduction Zone, Aotearoa New Zealand, From Seismic Reflection and Retro-Deformation Analysis. *Tectonics*, *43*(7). doi: https://doi.org/10.1029/2023TC008212

Tajima, F., & Célérier, B. (1989). Possible focal mechanism change during reactivation of a previously ruptured subduction zone and stress tensor implications. *Geophysical Journal International*, *98*(2), 301–316. doi: 10.1111/j.1365-246X.1989.tb03354.x

Thomas, C., Livermore, R., & Pollitz, F. (2003). Motion of the Scotia Sea plates. *Geophysical Journal International*, *155*(3), 789–804. doi: 10.1111/j.1365-246X.2003.02069.x

United States Geological Survey. (2025). *USGS Earthquake Event Page: us7000pwkn.* `https://earthquake.usgs.gov/earthquakes/eventpage/us7000pwkn`. (Accessed 21 January 2026)

Vuan, A., Sugan, M., & Plasencia Linares, M. P. (2014). A reappraisal of surface wave group velocity tomography in the Subantarctic Scotia Sea and surrounding ridges. *Global and Planetary Change*, *123*, 223–238. doi: 10.1016/j.gloplacha.2014.07.020

Wallace, L. M., Barnes, P., Beavan, J., Van Dissen, R., Litchfield, N., Mountjoy, J., ... Pondard, N. (2012). The kinematics of a transition from subduction to strike-slip: An example from the central New Zealand plate boundary. *Journal of Geophysical Research: Solid Earth*, *117*, B02405. doi: 10.1029/2011JB008640

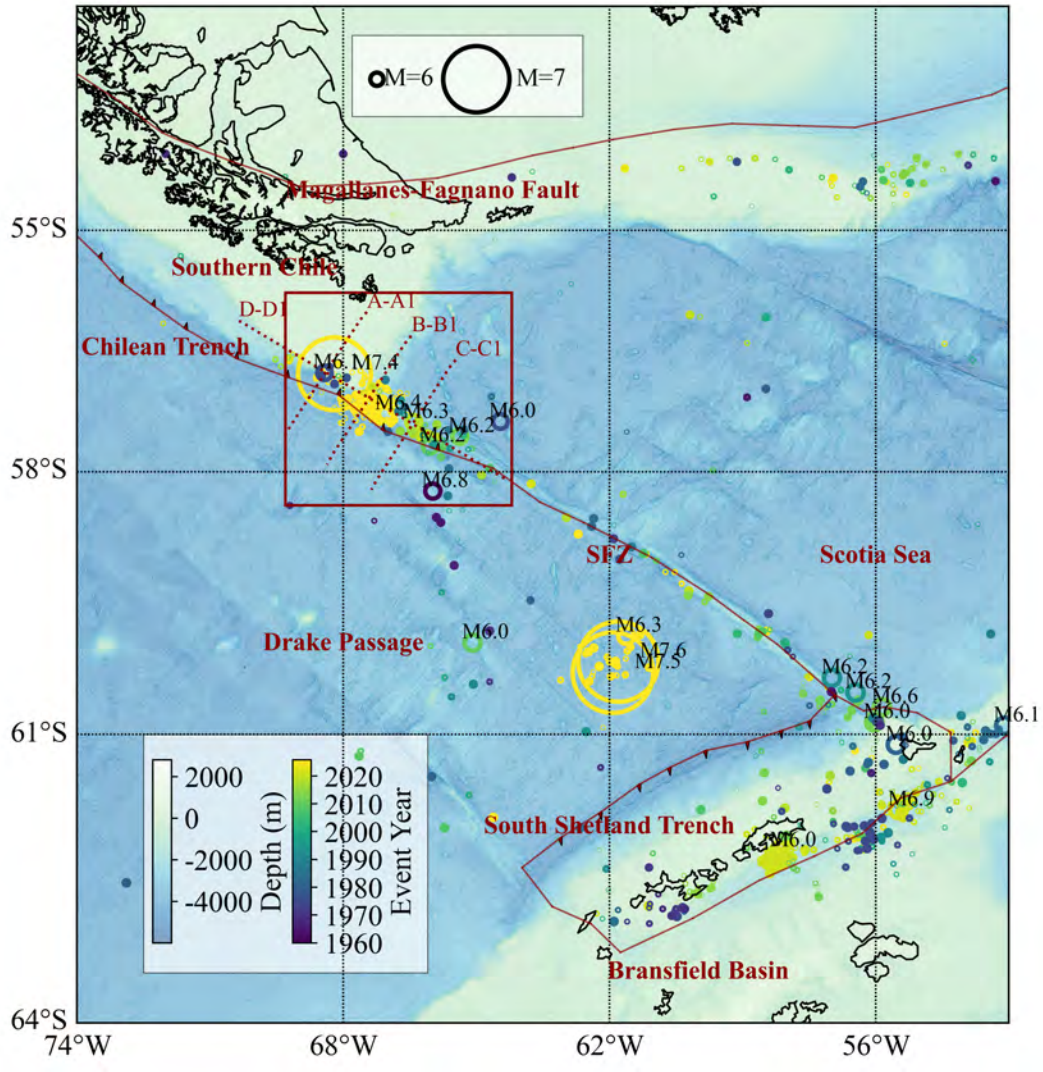


Figure 1. Main earthquakes from the ISC catalog and tectonic setting of the Drake Passage and southern Chilean margin. Bathymetry is shown with color shading, and earthquake epicenters are color-coded by year of occurrence (1960–2020). Major tectonic features include the Chilean Trench, the South Shetland Trench, and the Shackleton Fracture Zone (SFZ). Magnitudes for significant events (Mw $\geq$ 6.0) are plotted at their epicentral locations, with symbol size proportional to magnitude. The red box marks the study area, encompassing the Mw 7.4 mainshock and associated aftershocks. Plate boundaries and structural domains are indicated by red lines, and key geographic features such as the Drake Passage, Scotia Sea, and Bransfield Basin are labeled for reference.

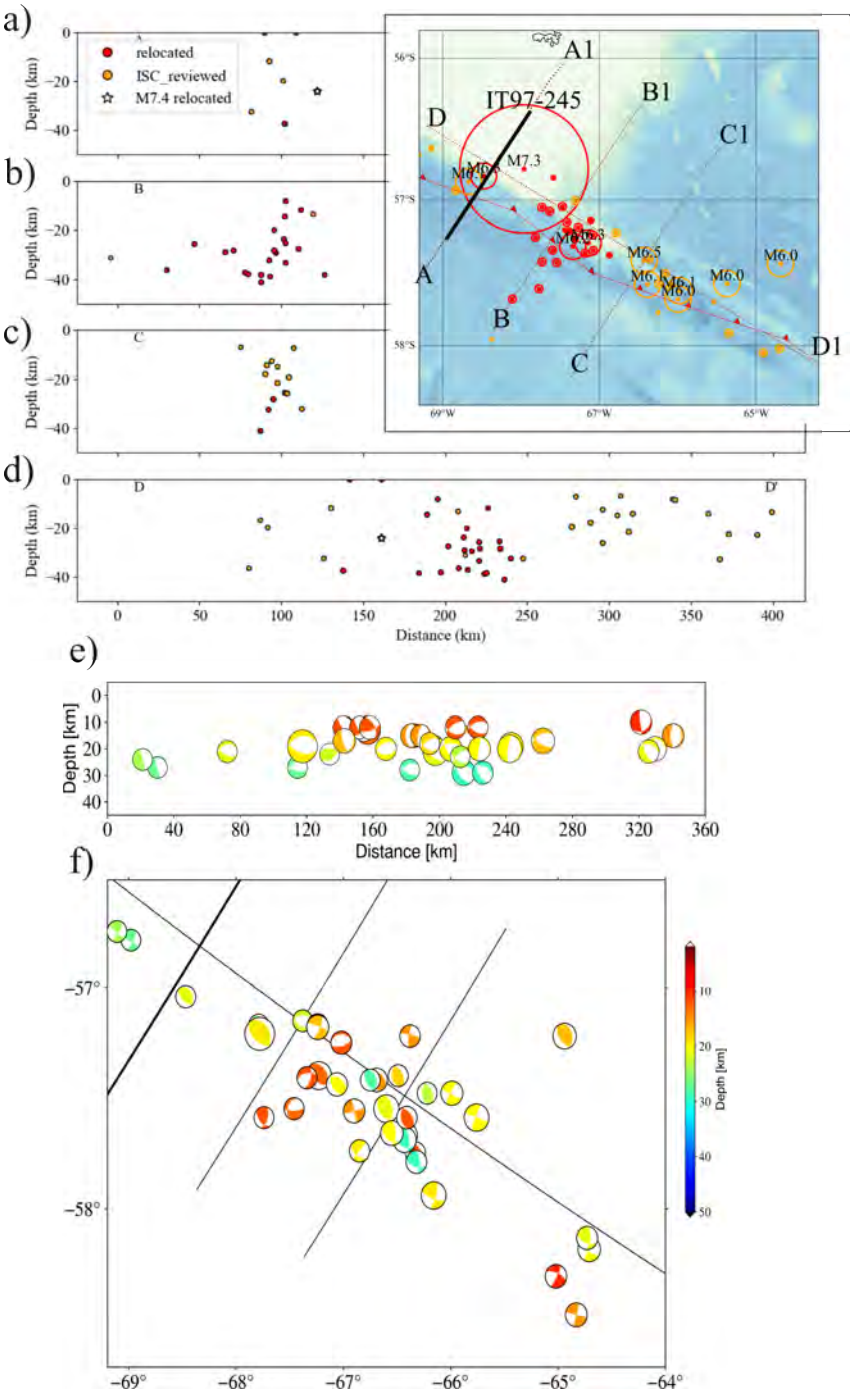


Figure 2. Cross sections and map views of seismicity associated with the May 2, 2025 earthquake. Relocated events (red) and pre-mainshock earthquakes from the ISC reviewed catalog (orange) are shown in (a) cross section A–A′, aligned with seismic reflection line IT97–245; (b) cross section B–B′, encompassing most aftershocks; and (c) cross section C–C′, illustrating events intersecting the Shackleton Fracture Zone (SFZ). Inset: Zoomed map of the red box in Figure 1 showing relocated events and ISC reviewed catalog earthquakes, with the cross-section traces indicated. (e) Depth view of focal mechanisms projected along profile D–D′ from the GCMT catalog. (f) Map view of focal mechanisms within the study area, color coded by depth.

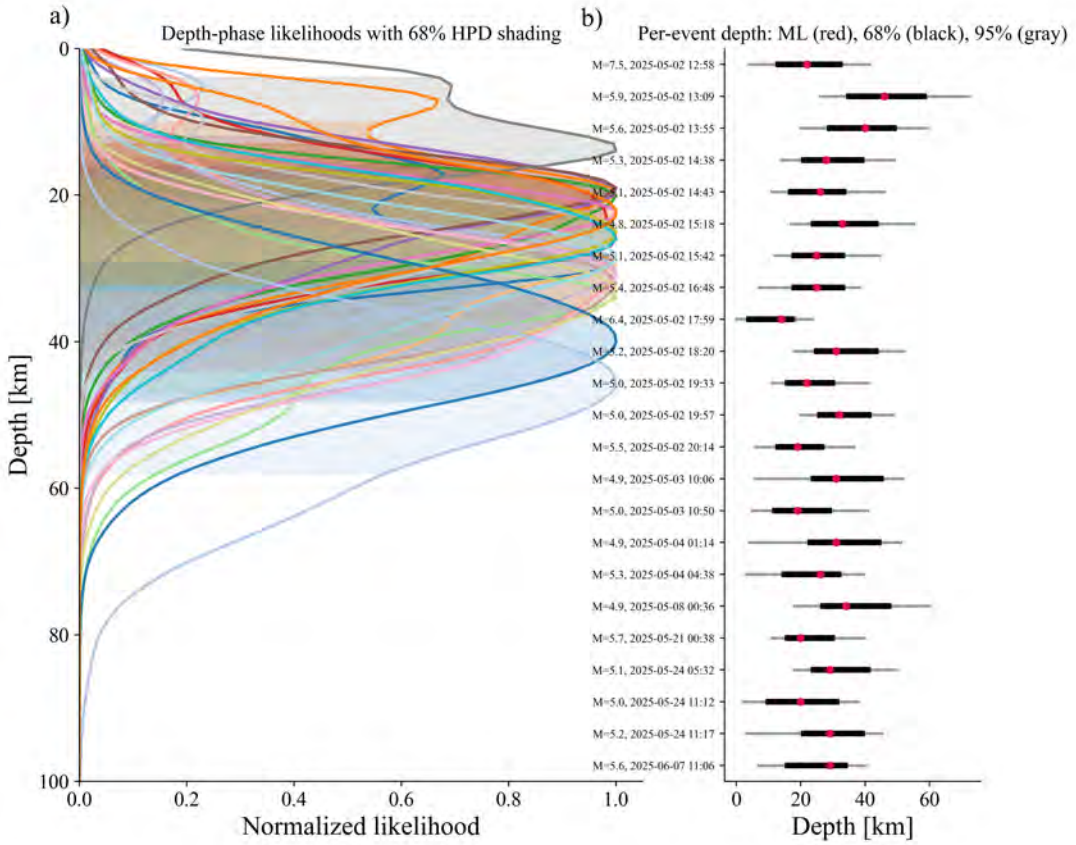


Figure 3. a) Normalized depth–phase likelihood functions for all analyzed events (left), computed from waveform-based depth-phase modeling using pP–P, sP–P, and related teleseismic depth-sensitive arrivals. For each event, the likelihood curve is shown together with its 68% highest posterior density (HPD) credible region, obtained via marginalization over phase picks and modeling uncertainties. Shading indicates the depth intervals where the posterior probability exceeds the 68% HPD threshold. b) Per-event depth solutions, including the maximum-likelihood (ML) depth estimate (red marker), 68% posterior credible interval (black bars), and 95% credible interval (gray bars). Events are ordered by origin time, and their magnitudes and timestamps are annotated accordingly. The reviewed centroid depth of the Mw 7.4 mainshock reported by the USGS is consistent with our estimate.

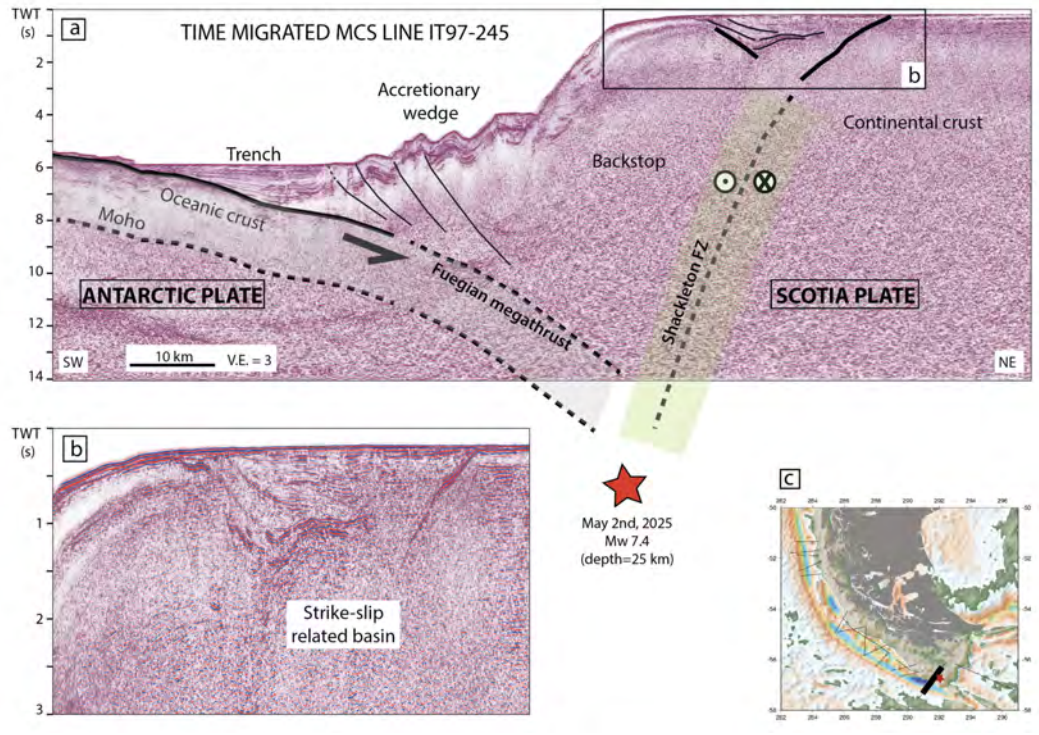


Figure 4. Seismic reflection profile IT97–245 crossing the southernmost Chilean margin, where the Chile Trench transitions into the Shackleton Fracture Zone (SFZ). (a) The profile illustrates the structural architecture of the plate boundary between the Antarctic and Scotia plates. The Fuegian megathrust (solid black line where imaged, dashed where interpreted) appears as a landward-dipping reflector beneath the accretionary wedge, marking the active subduction interface. Toward the northeast, a sedimentary basin develops where the SFZ impinges on the continental shelf, indicating significant deformation associated with the transform plate boundary system. The semi-vertical yellow zone marks the proposed deformation corridor of the Shackleton FZ, which accommodates oblique convergence and lateral displacement between plates. The transparent yellow area highlights the broader SFZ-related deformation zone, suggesting strain partitioning between thrust and strike-slip components consistent with oblique plate motion. The red star indicates the nucleation point of the May 2, 2025 mainshock (depth $\approx$ 25 km). (b) Zoomed view of the strike-slip–related basin, showing steeply dipping fault blocks and internal reflectors interpreted as syn-tectonic deposits formed under transtensional conditions during oblique plate motion. (c) Location map of seismic line IT97–245. The bold black line shows the segment of the profile interpreted in this work; thin black lines represent the dataset acquired in 1997 in Southern Chile and Antarctic. The uninterpreted seismic line is shown in Supplementary Figure S3.

The 2 May 2025 Mw 7.4 Drake Passage Earthquake: Insights into Tectonics at the Shackleton Fracture Zone–Chilean Trench Intersection

A. Vuan[1], G. Brancatelli[1], G. Brancolini[1], L. Gasperini[2], R. Geletti[1], E. Lodolo[1], A. Magrin[1], M. Menichetti[3], M. Plasencia[1], A. Polonia[2], M. Santulin[1], A. Tassone[4]

[1]Istituto Nazionale di Oceanografia e di Geofisica Sperimentale - OGS, Italy
[2]Istituto di Scienze Marine - CNR-ISMAR, Bologna, Italy
[3]Dipartimento di Scienze Pure ed Applicate, Università di Urbino, Urbino, Italy
[4]Instituto de Geociencias Básicas, Aplicadas y Ambientales de Buenos Aires (IGeBA), CONICET - Universidad de Buenos Aires, Argentina

Key Points:

- 1. Largest instrumentally recorded quake at the intersection of the Shackleton Fracture Zone and the Chilean Trench.
- 2. Seismic data show the mainshock nucleated at ~25 km depth, within the downdip portion of the megathrust interface.
- 3. Relocated earthquakes indicate a complex rupture involving the Chilean megathrust and Shackleton Fracture Zone structures.

Corresponding author: Alessandro Vuan, avuan@ogs.it

Abstract

On 2 May 2025, a Mw 7.4 earthquake occurred ~120 km off the southern tip of Tierra del Fuego, at the intersection of the Shackleton Fracture Zone and the Chilean Trench. This event is the largest recorded within this complex plate boundary, filling a gap between previous M>6 earthquakes. Most aftershocks exhibit compressional mechanisms with relatively steeply dipping planes, although some show strike-slip motion. To better resolve the activated fault system under limited station coverage, we relocated events and incorporated pP and pS phases identified using a trained classifier to constrain focal depths. Hypocentral depths range from ~15 to 35 km, with the mainshock nucleating at ~25 km. Aftershocks with predominantly reverse mechanisms cluster southeast of the mainshock along a steeply dipping structure near the Shackleton Fracture Zone. A 1997 multichannel seismic reflection profile crossing the epicentral region provides additional constraints on the possible complexity of the rupture process.

Plain Language Summary

On 2 May 2025, a magnitude 7.4 earthquake struck about 120 km off the southern tip of South America near Tierra del Fuego. It was the strongest earthquake ever recorded in this complex region where several tectonic plates meet. The event ruptured a well-recognized seismic gap separating earlier earthquakes near the junction of major fault systems, none of which exceeded magnitude 6.5. Aftershocks mostly showed compressional motion on steeply dipping faults, which is unusual for a typical plate-boundary megathrust rupture, and a few showed strike-slip motion. Because seismic stations are sparse in this area, advanced methods were used to improve earthquake locations. By identifying depth-sensitive seismic phases with a machine-learning model, we determined that the mainshock began about 25 km deep, consistent with the very small tsunami observed. Aftershocks southeast of the epicenter occurred on westward-dipping faults near the Shackleton Fracture Zone. Older seismic imaging data also help illuminate the complex fault system involved.

1 Introduction

The Mw 7.4 earthquake of May 2, 2025, occurred off the southernmost tip of Tierra del Fuego (Fig. 1) and represents the strongest event ever documented in this region, where the southern terminus of the South American convergent plate boundary merges into the Shackleton Fracture Zone (SFZ). The event was initially interpreted as a reverse-faulting earthquake with a fixed depth of 10 km (United States Geological Survey, 2025), and aftershock distributions were described as indicating a rupture propagating southeastward along the SFZ. The reviewed focal mechanism (United States Geological Survey, 2025) shows a dominantly compressional source, a centroid depth of 23.5 km, and a NW–SE–striking nodal plane dipping either 33° to the northeast or 57° to the southwest, which is unusually steep for a shallow megathrust event along an active subduction zone (Bradley & Hubbard, 2025). In addition, the non–double-couple (NDC) component is anomalously high (37%), suggesting that sparse station coverage, an inadequate velocity model, and/or a complex source process may contribute to this elevated value.

A maximum slip of approximately 4-5 m has been estimated from finite-fault inversion (United States Geological Survey, 2025; Ji et al., 2002). However, this estimate is strongly influenced by the use of teleseismic stations located far from the epicentral region, resulting in significant uncertainty. For example, the centroid depth derived from the focal mechanism (23.5 km) is inconsistent with the shallow asperity inferred from the finite-fault model (United States Geological Survey, 2025). Given the complex structural configuration of this segment of the South American margin—where convergence along the Chilean Trench merges into left-lateral strike-slip deformation along the SFZ—it remains unclear whether the 2025 earthquake primarily reflects subduction-related pro-

cesses or complex reverse slip along the transform system. Transitions from subduction to strike-slip faulting along plate boundaries can arise from geometric segmentation, termination of the plate interface, block rotations, and/or changes in relative plate-motion trajectories (Wallace et al., 2012).

In this study, we analyze seismological data together with an unpublished multichannel seismic reflection profile crossing the epicentral area to constrain the 2025 seismic sequence and the shallow crustal architecture of the continental margin off Tierra del Fuego. Epicentral locations of the mainshock and its aftershocks are refined using seismic data from the regional ASAIN network (Vuan et al., 2014; Plasencia Linares et al., 2021), with a particular focus on constraining hypocentral depths. This is achieved through the application of trained models capable of identifying depth-sensitive seismic phases such as pP and pS. The 1997 multichannel seismic profile resolves the shallow architecture of the subduction system and offers important constraints on the location and geometry of the plate interface and major faults potentially involved in the 2025 rupture.

2 Geodynamic and tectonic setting

Structural development offshore southernmost Chile is driven by the relative movements between the Antarctica, Scotia, and South America plates. The boundary between the Scotia and South America plates is marked by the Magallanes–Fagnano fault system and the North Scotia Ridge (Lodolo et al., 2002, 2003), whereas the Antarctic–Scotia plate boundary follows the Chilean Trench to the northwest and the SFZ toward the southeast (Fig. 1). The triple junction between these plates (the Fuegian triple junction of Polonia et al. (2007) has been interpreted as a diffuse deformation zone located where the Magallanes–Fagnano fault system projects toward the Chilean Trench (Forsyth, 1975; Cunningham, 1993). North of this area, subduction involves the Antarctic and South America plates, whereas south of the triple junction, convergence between the Antarctic and Scotia plates becomes progressively more oblique and transitions into the transcurrent motion of the SFZ.

Post-Miocene convergence processes are characterized by subduction between the Antarctic and Scotia plates at a rate of ~10-20 mm yr^{-1} (DeMets et al., 1990). Seismic reflection profiles reveal strong variations in frontal-wedge morphology, accretion rates, and overall structural style. These variations occur along oblique structural trends that segment the margin, driven by processes on the overriding plate as well as by local heterogeneities on the incoming plate, such as seamounts, fracture zones, and oceanic fabric (Polonia et al., 2007).

The intra-oceanic SFZ is a northwest–southeast trending fracture zone extending over 800 km from the southernmost Chilean Trench to the eastern termination of the South Shetland Trench, where it subducts beneath the South Shetland Islands block (Aldaya & Maldonado, 1996; Klepeis & Lawver, 1996).

Seismicity and focal mechanisms indicate that the SFZ is an active, left-lateral transpressive fault zone that, together with the South Scotia Ridge, accommodates relative motion between the Scotia and Antarctic plates (Pelayo & Wiens, 1989; Barker et al., 1991; Livermore et al., 1994; Aldaya & Maldonado, 1996; Galindo-Zaldívar et al., 1996; Klepeis & Lawver, 1996; Maldonado et al., 2000). Bathymetric (British Antarctic Survey, 2012; Bohoyo et al., 2016) and seismic data further reveal that the SFZ exhibits pronounced relief, and is flanked to the east by a well-developed trough system (Geletti et al., 2005).

South of the Chile Triple Junction (Fig. 1), seismicity along the margin is low (Pelayo & Wiens, 1989), which may be partly attributed to slow convergence rates (5-10 mm/year, and the obliquity of convergence that promotes strain partitioning (Lodolo et al., 2003;

Geletti et al., 2005; Polonia et al., 2007; Civile et al., 2012). Despite the limited seismicity—insufficient to resolve the slab geometry from earthquake data alone—seismic reflection profiles indicate that the continental margin between 50°S and 56°S is characterized by large folds and active thrust faults (Polonia et al., 1999, 2007). These features suggest that margin-perpendicular shortening is still active, or has slowed only recently (Rubio et al., 2000).

Overall, this geodynamic and tectonic environment diverges markedly from that of a classic subduction margin. It remains unclear how, in southernmost South America, the Chilean megathrust interacts with the SFZ and associated splay faults to generate large-magnitude earthquakes.

3 Materials and Methods

Our analysis of the 2 May 2025 Drake Passage earthquake sequence integrates regional and teleseismic seismology with multichannel seismic reflection data. We first relocated the mainshock and aftershocks using high-quality P and S phases from the Antarctic Seismographic Argentinean Italian Network (ASAIN) (Plasencia Linares et al., 2021) and selected global stations (Fig. S1 and Tab. S1), applying the LocSAT (Bratt & Nagy, 1991) algorithm with the IASPEI91 velocity model (Kennett & Engdahl, 1991) (see Supplementary Text S1).

To better constrain hypocentral depths, we identified pP and sP depth phases using machine-learning tools from the SeisBench framework (Münchmeyer et al., 2023), enabling probabilistic multi-station depth estimation despite sparse regional coverage (see Supplementary Text S2 and Fig. S2). Focal mechanisms were compiled from multiple international agencies (Dziewonski et al., 1981; Ekström et al., 2012) to assess fault geometry and stress orientation.

We further reprocessed (see Supplementary Text S3) a 1997 multichannel seismic line (Polonia et al., 2007) crossing the epicentral region to image crustal structure and plate-boundary architecture relevant to the rupture (Fig. S3).

4 Results and interpretation

4.1 Relocated hypocenters and depth distribution

The mean residuals of the P phases at the most frequently used stations are shown in Figure S4, while Table S2 summarizes the P and S phases employed in the relocation, together with the average time residuals, epicentral distances, and azimuths for each station. Stations located closest to the events consistently display negative residuals, indicating that observed P arrivals occurred earlier than the theoretical predictions. The major axis of the epicentral uncertainty ellipses is oriented roughly east–west, reflecting the sparser station coverage in that direction (Fig. S5). Horizontal location uncertainties range from approximately 5 km in the latitudinal direction to 15–20 km in the longitudinal direction, with the lower resolution in longitude primarily due to limited coverage in the Scotia Sea and Pacific Ocean.

Figure 2 presents cross sections and map views of seismicity associated with the May 2, 2025 earthquake sequence, combining relocated hypocenters with pre-mainshock events listed in the ISC reviewed catalog (Bondár & Storchak, 2011). The relocated hypocenters (red) and earlier ISC catalog earthquakes (orange) are projected onto three vertical profiles designed to illustrate the geometry of seismicity in the region. Profile A–A′ is aligned with seismic reflection line IT97–245 and highlights the distribution of earthquakes across the continental margin. Profile B–B′ encompasses most aftershocks and illustrates the spatial extent and depth range of the post-mainshock sequence. Profile C–

C′ captures events intersecting the Shackleton Fracture Zone (SFZ), providing insight into how this major structural boundary influences faulting patterns.

Depth estimates are improved by incorporating depth phases such as pP and sP, although identifying these phases is often challenging in this region due to high noise levels. Figure 3 shows the likelihood distributions and depth estimates for each event obtained using the *DeepPhaseNet* and *DepthPhaseTEAM* trained models (Münchmeyer et al., 2023). Both approaches yield internally consistent depth determinations across the sequence. Figure S2 illustrates the stations providing pP and sP picks for each event, demonstrating the dense azimuthal coverage that supports stable depth estimation.

Aftershocks predominantly occur between ~15 and 35 km depth, defining a tightly constrained seismogenic zone that spans the lower crust and uppermost mantle. Only one shallow event (M 5.1) lies above this interval. Notably, the centroid depth reported by the USGS for the Mw 7.4 mainshock closely matches our model-based estimate, reinforcing both the robustness of the inferred depth distribution and the consistency between independent methodologies.

An assessment of the robustness of pP–P-derived depths is shown in Figure S6, where observed delay times (Δt) are compared with parametric sensitivity curves describing how inferred depth depends on (a) the assumed crustal P-wave velocity V_p, (b) the P-wave takeoff angle θ, and (c) the thickness L of a shallow low-velocity layer (LVL). Depths derived from focal mechanisms shown in Figure 2 are consistent with those estimated using depth phases.

4.2 Mainshock and aftershock mechanisms

Despite variations in centroid depth reported across different catalogs (Table S3), the dips of the possible fault planes in the GCMT and USGS solutions appear to be well constrained, as does the compressive orientation of the rupture. For the mainshock, both nodal planes indicate dips ranging from 33° to 52° (Fig. 2b), considerably steeper than the ∼5°–20° dip expected for the shallow Chilean megathrust. This suggests that the rupture likely occurred within one of the tectonic plates rather than along the plate interface, or that the rupture may be composite, involving multiple structures.

Analysis of historical focal mechanisms from the GCMT catalog since 1976 shows that dip angles in this region are consistently greater than 34° (Table S4). Similarly, Pelayo and Wiens (1989) reported two mb > 6.0 earthquakes in 1975 and 1976 with compressional mechanisms and dips exceeding 40°. Few early aftershocks exhibit strike-slip mechanisms with centroid depths of approximately 15 km (Table S5). Rose diagrams of P-axes (orientations ∼45°–60°, maximum compression) and T-axes (∼135°–150°, maximum tension) derived from these focal solutions are shown in the supplementary material (Fig. S7).

Taken together, these observations indicate a predominantly steeply dipping rupture. Nevertheless, given the compressional nature of the mainshock and its close proximity to the subduction interface, a contribution from the megathrust cannot be excluded, either in the form of direct slip or stress transfer to adjacent faults.

4.3 Seismic reflection profile and crustal structure

The time-migrated multichannel seismic line IT97–245 trends approximately orthogonal to the southernmost Chilean subduction system, extending from the oceanic trench to the continental shelf and passing near the epicenter of the May 2, 2025 earthquake (Figs. 1 and 2; profile A–A′). The Antarctic–Scotia plate boundary region is imaged to approximately 14 s two-way travel time (TWT). In the outer domain of the subduction system, the top of the Antarctic Plate oceanic basement dips landward, and the

oceanic crust is underlain at depth by the Moho reflector (Fig. 4a). The seafloor in the trench domain is relatively flat because the oceanic basement is buried beneath sediment infill at the trench axis. The accretionary wedge is about 20 km wide and is composed of deformed sediments scraped off the subducting Antarctic Plate and accreted along landward-dipping thrust faults that sole out against the main detachment.

Within the continental shelf, a well-developed sedimentary basin is clearly imaged (Fig. 4b). The basin depocenter contains a sedimentary section up to ∼2 s TWT thick. The location of this basin coincides with the northwestward continuation of the Shackleton Fracture Zone (SFZ), suggesting that the SFZ exerts a first-order control on the tectonic evolution of the region.

5 Discussion

The area where the Mw 7.4 earthquake occurred includes: (i) the southern end of the Andean subduction zone, where the interaction between the continental margin of Tierra del Fuego and the oceanic crust of the Antarctic Plate is highly oblique, and (ii) the northern termination of the left-lateral SFZ. Fault-plane solutions indicate a reverse mechanism for the May 2, 2025 mainshock, with a NE- or SW-dipping fault geometry. The nodal planes inferred near the trench ($\mathrm{dip}_1 > 35^\circ$ and $\mathrm{dip}_2 \approx 55$–$60^\circ$) are unusually steep for an Andean-type, shallow-dipping megathrust. Moreover, the temporal and spatial variation of dip angles (Fig. S8) reveals predominantly steep fault geometries, consistent with rupture along a relatively high-angle structure that may reflect the influence of oblique convergence and local tectonic segmentation.

Alternatively, such geometries may indicate: (1) a splay fault within the overriding plate that accommodates compressive stresses related to accretion; (2) rupture within a transition zone where the subducting slab begins to steepen; or (3) a composite source in which the mainshock triggered slip along one or more segments forming the northernmost part of the SFZ. Supporting evidence for a composite rupture is provided by morpho-bathymetric data (British Antarctic Survey, 2012; Bohoyo et al., 2016), which show that the SFZ bifurcates into at least two ridges to the north that parallel its main trace and extend onto the southern Tierra del Fuego continental shelf (Bohoyo et al., 2019). Similar morphologies occur along oceanic transverse ridges, such as those imaged across the Romanche and Vema fracture zones (Bonatti et al., 1994, 2005). The approximately east–west-directed stress regime in the Drake Passage region (Thomas et al., 2003) is largely dissipated along a narrow deformation zone within the SFZ, which is interpreted to result from crustal uplift and shortening (Geletti et al., 2005) and accommodates much of the present-day Antarctic–Scotia plate motion. Taken together, these observations support the activation of a composite source in which the megathrust interacts with the SFZ through transpressional and transtensional mechanisms, as also suggested by the distribution of aftershock seismicity.

The distribution of focal epicenters, which trend predominantly NW–SE, further supports this interpretation. The sedimentary basin imaged on the continental shelf in line IT97–245 (Fig. 4b) closely resembles other shelf basins along the western termination of the South America–Scotia plate boundary, where the Magallanes–Fagnano transform fault (Lodolo et al., 2003) intersects the southern Chilean Trench. In that region, a ∼3 km-thick sedimentary depocenter (the Madre de Dios Basin; (González, 1989)) develops (Polonia et al., 2007, their Fig. 6b), illustrating strong interaction between transform faulting and subduction processes.

The inversion of the mainshock focal mechanism in the USGS catalog reveals a 37% non–double-couple (NDC) component. Composite ruptures involving multiple fault types commonly generate large NDC values, which can range from negligible in simple settings to 20–48% in structurally complex environments (Tajima & Célérier, 1989; Frohlich &

Apperson, 1992; Ekström & Engdahl, 1989). Kuge and Kawakatsu (1992) showed that superposition of double-couple sources with rotating principal axes can produce significant NDC components. On a global scale, earthquakes with Mw > 6.5 in the GCMT catalog typically exhibit smaller NDC values (∼17%) (Rösler et al., 2021, 2023) than that inferred for the 2025 mainshock (37%), suggesting unresolved complexity in the source process.

The SFZ and related tectonic discontinuities within the incoming oceanic lithosphere can strongly perturb slab geometry and subduction processes along an active margin. Mechanical weakening along these discontinuities, combined with bending-related faulting, reduces effective strength and modifies slab buoyancy, promoting segmentation, tearing, and along-strike variations in subduction geometry. These processes influence interface coupling and stress transmission, resulting in spatially variable seismicity patterns and along-strike slab heterogeneity (Rodríguez et al., 2024). Based on these elements, we propose a kinematic scenario in which the mainshock nucleated between the obliquely subducting Antarctic Plate and the overriding Scotia Plate, within a highly heterogeneous crustal and upper-mantle structure. At subduction–transform transitions, the geometry of the plate interface may steepen abruptly over short distances or involve splay faults that appear steep in focal mechanisms. Composite sources involving contributions from megathrust patches, upper-plate reverse faults, and the SFZ can also produce steep nodal planes and large NDC values.

The event also generated transpressive stress at the intersection between the trench and the northern segment of the SFZ, where trench-normal and trench-parallel forces interact. This is the zone where oblique subduction transitions into strike-slip motion, and the convergence vector partitions into perpendicular and parallel components relative to the trench. In this complex structural scenario, portions of the overriding plate appear to be offset with respect to the SFZ trench-parallel strike, producing shallow faults that likely may move independently.

Similar transition zones occur along the New Zealand Hikurangi margin leading into the Alpine Fault system (Stevens et al., 2024), and in Sumatra where oblique convergence between the Indo-Australian and Eurasian plates is accommodated by the right-lateral Great Sumatran Fault (McNeill & Henstock, 2014; Moeremans et al., 2014).

6 Conclusions

Relocated hypocenters in the Drake Passage region indicate that seismogenic activity generally occurs between 15 km and approximately 35 km depth, consistent across both deep-learning–based approaches and traditional relocations using nearby regional stations. The May 2, 2025 mainshock nucleated at roughly 25 km depth.

Horizontal location uncertainties are larger in longitude due to sparse station coverage in the Scotia Sea, ranging from about 5 km to 20 km. Depth estimates constrained by pP and sP phases agree with depths reported for pre-2024 events in the ISC-reviewed bulletin located near the aftershock zone.

The depth distribution of seismicity, focal mechanism solutions, and structural constraints suggests that the mainshock originated in the interaction zone between a southwest-dipping structure associated with the SFZ and the Chilean megathrust. The predominantly compressional mechanisms with relatively steep dips, together with the clustering of aftershocks in the lower crust and upper mantle, support a composite rupture in which slip was partitioned across multiple fault segments.

Additional support comes from the multichannel seismic reflection profile, which clearly images the complex structural interaction between the shallow Chilean megathrust and the SFZ in the immediate vicinity of the Mw 7.4 hypocenter.

Open Research Section

All data used in this study are publicly available and properly cited in the references and supporting material.

Waveform and metadata used for event relocation and depth–phase analysis were obtained from the Antarctic Seismographic Argentinean Italian Network (ASAIN) and selected FDSN global stations (see Table S1 and Fig. S1 for station list and usage details). Data can be accessed at the EarthScope Data Center (IRIS DMC): `https://service.earthscope.org/fdsnws/dataselect/1/`, and at the ORFEUS Data Center (ORFEUS): `http://www.orfeus-eu.org/fdsnws/dataselect/1/`.

Regional catalog and focal–mechanism data prior to the mainshock were obtained from the International Seismological Centre (ISC) Reviewed Bulletin: `https://www.isc.ac.uk/iscbulletin/search/catalogue/`. Global Centroid Moment Tensor (GCMT) solutions were retrieved from `http://www.globalcmt.org`.

Source parameters and centroid solutions for the 2 May 2025 Drake Passage mainshock (Mw 7.4) were accessed from the USGS Earthquake Event Page: `https://earthquake.usgs.gov/earthquakes/eventpage/us7000pwkn` (accessed 21 January 2026).

Bathymetric grids used in Figures 1–2 derive from the General Bathymetric Chart of the Oceans (GEBCO): `https://www.gebco.net/data-products/gridded-bathymetry-data` (accessed 21 January 2026).

Seismic reflection data along line IT97–245 were reprocessed for this study; interpreted and uninterpreted seismic sections are provided as Figure 4 and Figure S3 in Supporting Information.

Software used for routine processing includes SeisComP (GFZ & Gempa GmbH, DOI: 10.5880/GFZ.2.4.2020.003). SeisComP relocation parameters are provided in Table S2 (Supporting Information). Depth–phase identification employed the SeisBench deep–learning models referenced in the manuscript and available at `https://zenodo.org/records/5568813`.

The derived relocated catalog is provided in QuakeML(https://quake.ethz.ch/quakeml) format as a supplementary file (events.qml).

All resources above are openly available or preserved in trusted repositories with persistent identifiers, in accordance with AGU policy requiring that data and code needed to understand, evaluate, and build upon the results be accessible at the time of review and publication.

Conflict of Interest declaration

The authors declare there are no conflicts of interest for this manuscript.

Acknowledgments

We thank the institutions and data providers that made this research possible. Seismic data were provided by the Antarctic Seismographic Argentinean Italian Network (ASAIN) and the International Seismological Centre (ISC). Bathymetric data were obtained from the British Antarctic Survey. We acknowledge the use of the SeisComP package (GFZ & Gempa GmbH, 2008). This work was supported by the Italian Programma Nazionale di Ricerche in Antartide (PNRA). We thank A. Camerlenghi for enabling the acquisition of the seismic line during the return from the Antarctic Peninsula, which took place over several days of fair weather, a rare condition at these latitudes. The authors acknowledge the scientific and logistic support of Dirección Nacional del Antártico (DNA) – In-

stituto Antártico Argentino (IAA) and the fundamental role of the Armada, Ejército, and Fuerza Aérea Argentina personnel in creating and maintaining the proper operating conditions for the ASAIN stations in the Antarctic bases.

References

Aldaya, F., & Maldonado, A. (1996). Tectonics of the triple junction at the southern end of the Shackleton Fracture Zone (Antarctic Peninsula). *Geo-Marine Letters*, *16*, 279–286. doi: 10.1007/BF01245558

Barker, P. F., Dalziel, I. W. D., & Storey, B. C. (1991). Tectonic development of the Scotia Arc region. In R. J. Tingey (Ed.), *The geology of antarctica* (pp. 215–248). Oxford: Clarendon Press.

Bohoyo, F., Larter, R. D., Galindo-Zaldívar, J., Leat, P. T., Maldonado, A., Tate, A. J., & Riley, T. R. (2019). Morphological and geological features of Drake Passage, Antarctica, from a new digital bathymetric model. *Journal of Maps*, *15*(2), 49–59. doi: 10.1080/17445647.2018.1543618

Bohoyo, F., Larter, R. D., Galindo-Zaldívar, J., Leat, P. T., Maldonado, A., Tate, A. J., ... Riley, T. R. (2016). *Bathymetry and geological setting of the Drake Passage* (BAS GEOMAP 2 Series). Cambridge: British Antarctic Survey.

Bonatti, E., Brunelli, D., Buck, W. R., Cipriani, A., Fabretti, P., Ferrante, V., ... Ligi, M. (2005). Flexural uplift of a lithospheric slab near the vema transform (Central Atlantic): Timing and mechanisms. *Earth and Planetary Science Letters*, *240*(3–4), 642–655. doi: 10.1016/j.epsl.2005.10.010

Bonatti, E., Ligi, M., Gasperini, L., Peyve, A., Raznitsin, Y., & Chen, Y. J. (1994). Transform migration and vertical tectonics at the Romanche fracture zone, equatorial Atlantic. *Journal of Geophysical Research: Solid Earth*, *99*(B11), 21779–21802. doi: 10.1029/94JB01178

Bondár, I., & Storchak, D. A. (2011). Improved location procedures at the international seismological centre. *Geophysical Journal International*, *186*, 1220–1244. doi: 10.1111/j.1365-246X.2011.05107.x

Bradley, K., & Hubbard, J. (2025). Unusual m7.4 earthquake strikes south of south america. *Earthquake Insights*. doi: 10.62481/0b850b61

Bratt, S. R., & Nagy, W. (1991). *The LocSAT Program* (Tech. Rep.). San Diego, CA: Science Applications International Corporation (SAIC). (User manual/report)

British Antarctic Survey. (2012). *High-resolution bathymetric data of the Shackleton Fracture Zone.* `https://www.bas.ac.uk/data/our-data/maps`. (Accessed Jan 21, 2026)

Civile, D., Lodolo, E., Vuan, A., & Loreto, M. F. (2012). Tectonics of the Scotia–Antarctica plate boundary constrained from seismic and seismological data. *Tectonophysics*, *550–553*, 17–34. doi: 10.1016/j.tecto.2012.05.002

Cunningham, W. D. (1993). Strike-slip faults in the southernmost Andes and the development of the Patagonian orocline. *Tectonics*, *12*(1), 169–186. doi: 10.1029/92TC01790

DeMets, C., Gordon, R. G., Argus, D. F., & Stein, S. (1990). Current plate motions. *Geophysical Journal International*, *101*, 425–478. doi: 10.1111/j.1365-246X.1990.tb06579.x

Dziewonski, A. M., Chou, T.-A., & Woodhouse, J. H. (1981). Determination of earthquake source parameters from waveform data for studies of global and regional seismicity. *Journal of Geophysical Research: Solid Earth*, *86*(B4), 2825–2852. doi: 10.1029/JB086iB04p02825

Ekström, G., & Engdahl, E. R. (1989). Earthquake source parameters and stress distribution in the Adak Island region of the central Aleutian Islands, Alaska. *Journal of Geophysical Research: Solid Earth*, *94*(B11), 15499–15519. doi: 10.1029/JB094iB11p15499

Ekström, G., Nettles, M., & Dziewonski, A. M. (2012). The global CMT project 2004–2010: Centroid-moment tensors for 13,017 earthquakes. *Physics of the Earth and Planetary Interiors*, *200–201*, 1–9. doi: 10.1016/j.pepi.2012.04.002

Forsyth, D. W. (1975). Fault plane solutions and tectonics of the South Atlantic and Scotia Sea. *Geophysical Journal International*, *80*, 1429–1443. doi: 10.1029/JB080i011p01429

Frohlich, C., & Apperson, K. D. (1992). Earthquake focal mechanisms, moment tensors, and the consistency of seismic activity near plate boundaries. *Tectonics*, *11*(2), 279–296. doi: 10.1029/91TC02888

Galindo-Zaldívar, J., Jabaloy, A., Maldonado, A., & Sanz de Galdeano, C. (1996). Continental fragmentation along the South Scotia Ridge transcurrent plate boundary (NE Antarctic Peninsula). *Tectonophysics*, *258*, 275–301. doi: 10.1016/0040-1951(95)00211-1

Geletti, R., Lodolo, E., Schreider, A. A., & Polonia, A. (2005). Seismic structure and tectonics of the Shackleton Fracture Zone (Drake Passage, Scotia Sea). *Marine Geophysical Research*, *26*, 17–28. doi: 10.1007/s11001-005-0147-4

GFZ, & Gempa GmbH. (2008). *The SeisComP seismological software package.* GFZ Data Services. doi: 10.5880/GFZ.2.4.2020.003

González, E. (1989). Hydrocarbon resources in the coastal zone of Chile. In G. E. Ericksen, M. T. Ganas Pinochet, & J. A. Reinemund (Eds.), *Geology of the andes and its relation to hydrocarbon and mineral resources* (Vol. 11, pp. 383–404). Houston, Texas: Circum-Pacific Council for Energy and Mineral Resources.

Ji, C., Wald, D. J., & Helmberger, D. V. (2002). Source description of the 1999 Hector Mine, California, earthquake. Part I: Wavelet domain inversion theory and resolution analysis. *Bulletin of the Seismological Society of America*, *92*(4), 1192–1207. doi: 10.1785/0120000916

Kennett, B. L. N., & Engdahl, E. R. (1991). Traveltimes for global earthquake location and phase identification. *Geophysical Journal International*, *105*(2), 429–465. doi: 10.1111/j.1365-246X.1991.tb06724.x

Klepeis, K. A., & Lawver, L. A. (1996). Tectonics of the Antarctic–Scotia plate boundary near Elephant and Clarence Islands, West Antarctica. *Journal of Geophysical Research: Solid Earth*, *101*(B9), 20211–20231. doi: 10.1029/96JB01510

Kuge, K., & Kawakatsu, H. (1992). Deep and intermediate-depth non-double-couple earthquakes: Interpretation of moment tensor inversions using various passbands of very broadband seismic data. *Geophysical Journal International*, *111*(3), 589–606. doi: 10.1111/j.1365-246X.1992.tb02114.x

Livermore, R., McAdoo, D., & Marks, K. (1994). Scotia Sea tectonics from high-resolution satellite gravity. *Earth and Planetary Science Letters*, *123*(1–3), 255–268. doi: 10.1016/0012-821X(94)90272-0

Lodolo, E., Menichetti, M., Bartole, R., Ben-Avraham, Z., Tassone, A., & Lippai, H. (2003). Magallanes–Fagnano continental transform fault (Tierra del Fuego, southernmost South America). *Tectonics*, *22*, 1076. doi: 10.1029/2003TC001500

Lodolo, E., Menichetti, M., Tassone, A., Geletti, R., Sterzai, P., Lippai, H., & Hormaechea, H.-L. (2002). Researchers target a continental transform fault in Tierra del Fuego. *Eos, Transactions American Geophysical Union*, *83*, 5–61. doi: 10.1029/2002EO000001

Maldonado, A., Carlos Balanyá, J., Barnolas, A., Galindo-Zaldívar, J., Hernández, J., Jabaloy, A., ... Viseras, C. (2000). Tectonics of an extinct ridge-transform intersection, Drake Passage (Antarctica). *Marine Geophysical Researches*, *21*, 43–68. doi: 10.1023/A:1004762311398

McNeill, L. C., & Henstock, T. J. (2014). Forearc structure and morphology along the Sumatra–Andaman subduction zone. *Tectonics*, *33*(2), 112–134. doi: 10

.1002/2012TC003264

Moeremans, R., Singh, S. C., Mukti, M., McArdle, J., & Johansen, K. (2014). Seismic images of structural variations along the deformation front of the Andaman–Sumatra subduction zone: Implications for rupture propagation and tsunamigenesis. *Earth and Planetary Science Letters*, *386*, 75–85. doi: 10.1016/j.epsl.2013.11.003

Münchmeyer, J., Saul, J., & Tilmann, F. (2023). Learning the Deep and the Shallow: Deep-Learning-Based Depth Phase Picking and Earthquake Depth Estimation. *Seismological Research Letters*, *95*(3), 1543–1557. doi: 10.1785/0220230187

Pelayo, A. M., & Wiens, D. A. (1989). Seismotectonics and relative plate motions in the Scotia Sea region. *Journal of Geophysical Research: Solid Earth*, *94*(B6), 7293–7320. doi: 10.1029/JB094iB06p07293

Plasencia Linares, M. P., Cravos, C., Laterza, R., Bernardi, P., Comelli, P., Grossi, M., ... Parolai, S. (2021). The Antarctic Seismographic Argentinean Italian Network (ASAIN): Recording Earthquakes in the Scotia Sea Region. *Seismological Research Letters*, *92*(5), 748–2757. doi: 10.1785/0220200484

Polonia, A., Brancolini, G., Torelli, L., & Vera, E. (1999). Structural variability at the active continental margin off southernmost Chile. *Journal of Geodynamics*, *27*, 289–307. doi: 10.1016/S0264-3707(98)00003-9

Polonia, A., Torelli, L., Brancolini, G., & Loreto, M.-F. (2007). Tectonic accretion versus erosion along the southern Chile trench: Oblique subduction and margin segmentation. *Tectonics*, *26*, TC3005. doi: 10.1029/2006TC001983

Rodríguez, E. E., Beck, S. L., Ruiz, M., Meltzer, A., Portner, D. E., Hernández, S., ... Charvis, P. (2024). Seismic imaging of the Northern Andean subduction zone from teleseismic tomography: A torn and fragmented Nazca slab. *Geophysical Journal International*, *236*, 593–606. doi: 10.1093/gji/ggad421

Rösler, B., Stein, S., & Spencer, B. D. (2021). Uncertainties in Seismic Moment Tensors Inferred from Differences Between Global Catalogs. *Seismological Research Letters*, *92*(6), 3698–3711. doi: 10.1785/0220210066

Rösler, B., Stein, S., & Spencer, B. D. (2023). When Are Non-Double-Couple Components of Seismic Moment Tensors Reliable? *Seismica*, *2*(1). doi: 10.26443/seismica.v2i1.241

Rubio, E., Torné, M., Vera, E., & Díaz, A. (2000). Crustal structure of the southernmost Chilean margin from seismic and gravity data. *Tectonophysics*, *323*(1–2), 39–60. doi: 10.1016/S0040-1951(00)00101-3

Stevens, D. E., McNeill, L. C., Henstock, T. J., Barnes, P. M., Crutchley, G., Bangs, N., ... Van Avendonk, H. J. A. (2024). Structural Variation Along the Southern Hikurangi Subduction Zone, Aotearoa New Zealand, From Seismic Reflection and Retro-Deformation Analysis. *Tectonics*, *43*(7). doi: https://doi.org/10.1029/2023TC008212

Tajima, F., & Célérier, B. (1989). Possible focal mechanism change during reactivation of a previously ruptured subduction zone and stress tensor implications. *Geophysical Journal International*, *98*(2), 301–316. doi: 10.1111/j.1365-246X.1989.tb03354.x

Thomas, C., Livermore, R., & Pollitz, F. (2003). Motion of the Scotia Sea plates. *Geophysical Journal International*, *155*(3), 789–804. doi: 10.1111/j.1365-246X.2003.02069.x

United States Geological Survey. (2025). *USGS Earthquake Event Page: us7000pwkn.* `https://earthquake.usgs.gov/earthquakes/eventpage/us7000pwkn`. (Accessed 21 January 2026)

Vuan, A., Sugan, M., & Plasencia Linares, M. P. (2014). A reappraisal of surface wave group velocity tomography in the Subantarctic Scotia Sea and surrounding ridges. *Global and Planetary Change*, *123*, 223–238. doi: 10.1016/j.gloplacha.2014.07.020

Wallace, L. M., Barnes, P., Beavan, J., Van Dissen, R., Litchfield, N., Mountjoy, J., ... Pondard, N. (2012). The kinematics of a transition from subduction to strike-slip: An example from the central New Zealand plate boundary. *Journal of Geophysical Research: Solid Earth*, *117*, B02405. doi: 10.1029/2011JB008640

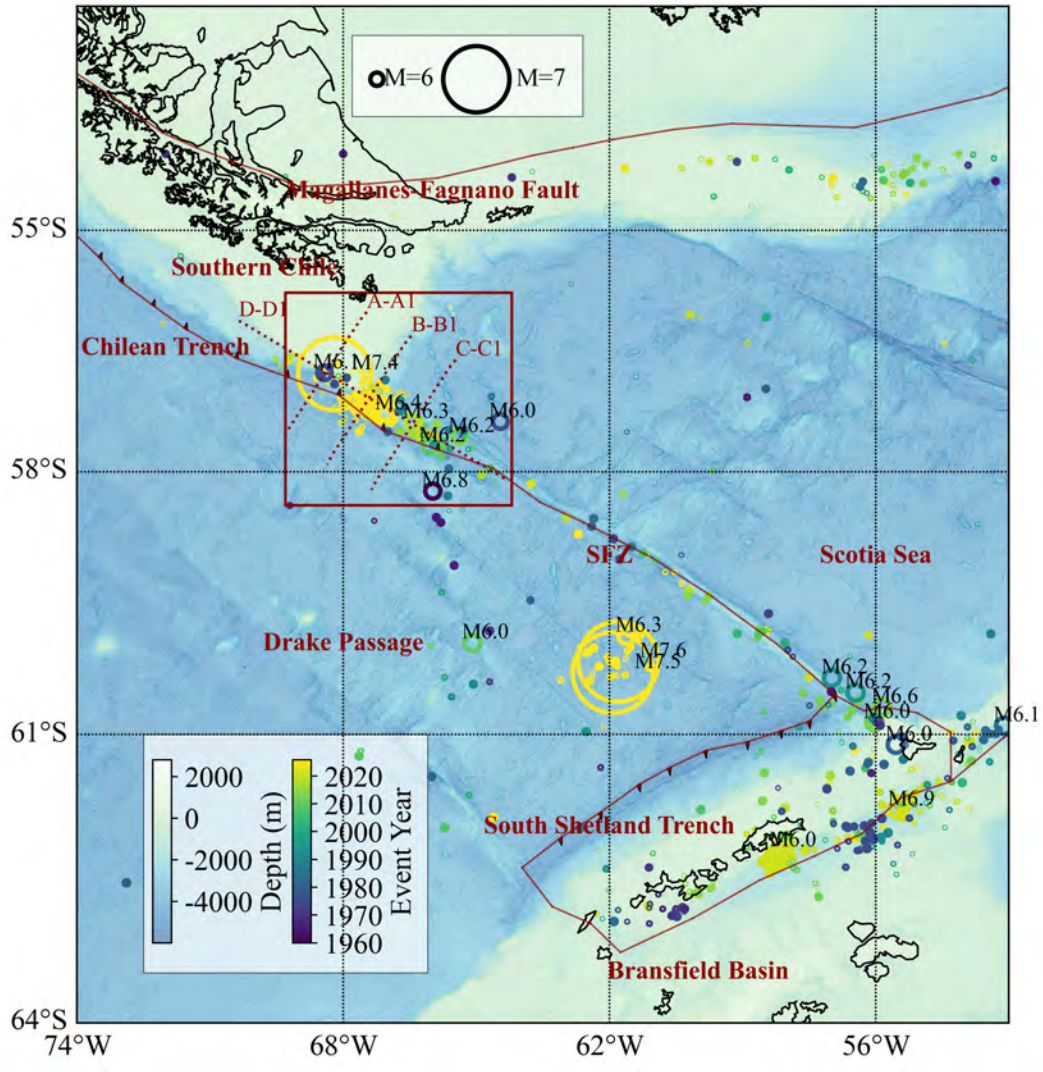


Figure 1. Main earthquakes from the ISC catalog and tectonic setting of the Drake Passage and southern Chilean margin. Bathymetry is shown with color shading, and earthquake epicenters are color-coded by year of occurrence (1960–2020). Major tectonic features include the Chilean Trench, the South Shetland Trench, and the Shackleton Fracture Zone (SFZ). Magnitudes for significant events (Mw $\geq$ 6.0) are plotted at their epicentral locations, with symbol size proportional to magnitude. The red box marks the study area, encompassing the Mw 7.4 mainshock and associated aftershocks. Plate boundaries and structural domains are indicated by red lines, and key geographic features such as the Drake Passage, Scotia Sea, and Bransfield Basin are labeled for reference.

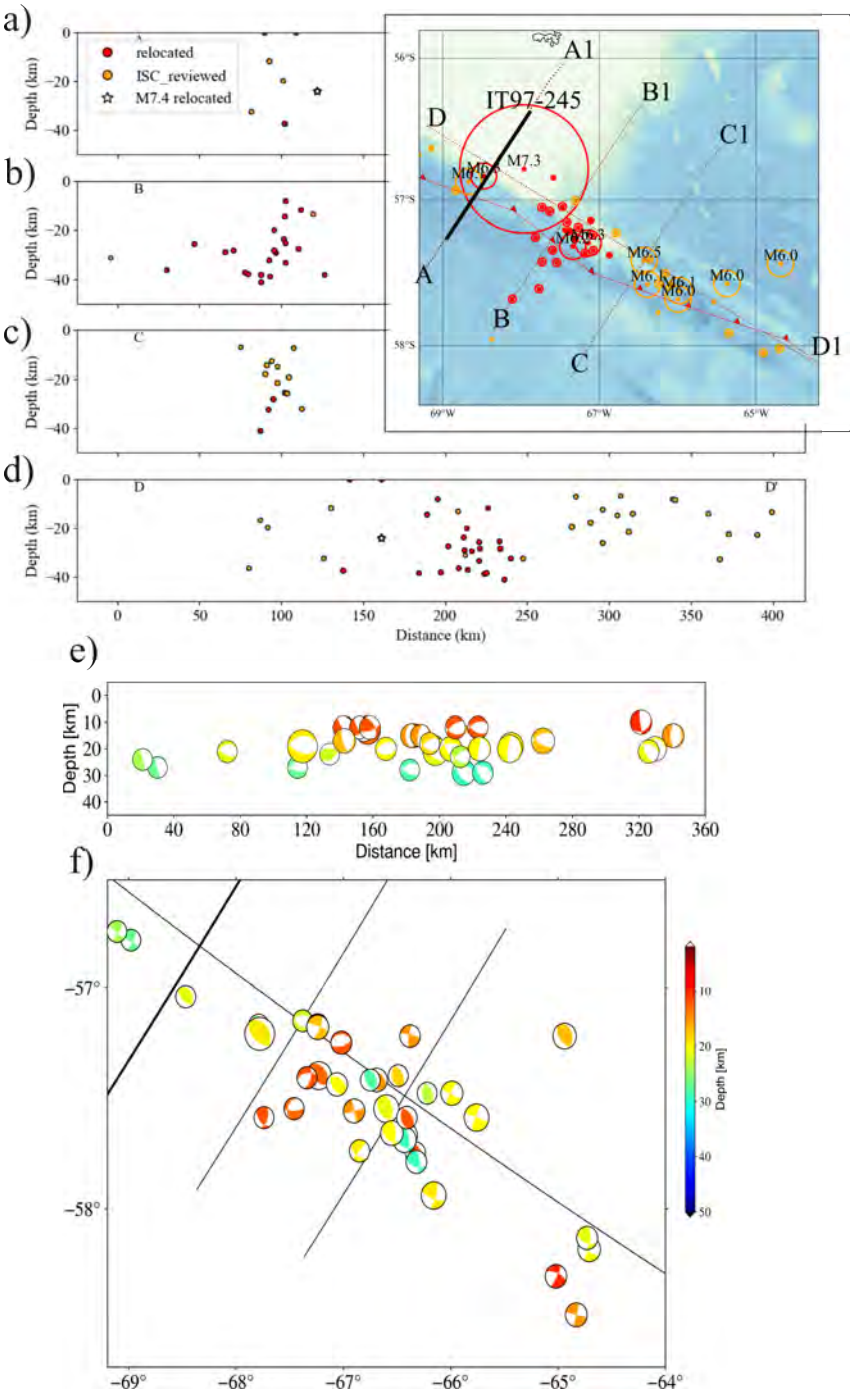


Figure 2. Cross sections and map views of seismicity associated with the May 2, 2025 earthquake. Relocated events (red) and pre-mainshock earthquakes from the ISC reviewed catalog (orange) are shown in (a) cross section A–A′, aligned with seismic reflection line IT97–245; (b) cross section B–B′, encompassing most aftershocks; and (c) cross section C–C′, illustrating events intersecting the Shackleton Fracture Zone (SFZ). Inset: Zoomed map of the red box in Figure 1 showing relocated events and ISC reviewed catalog earthquakes, with the cross-section traces indicated. (e) Depth view of focal mechanisms projected along profile D–D′ from the GCMT catalog. (f) Map view of focal mechanisms within the study area, color coded by depth.

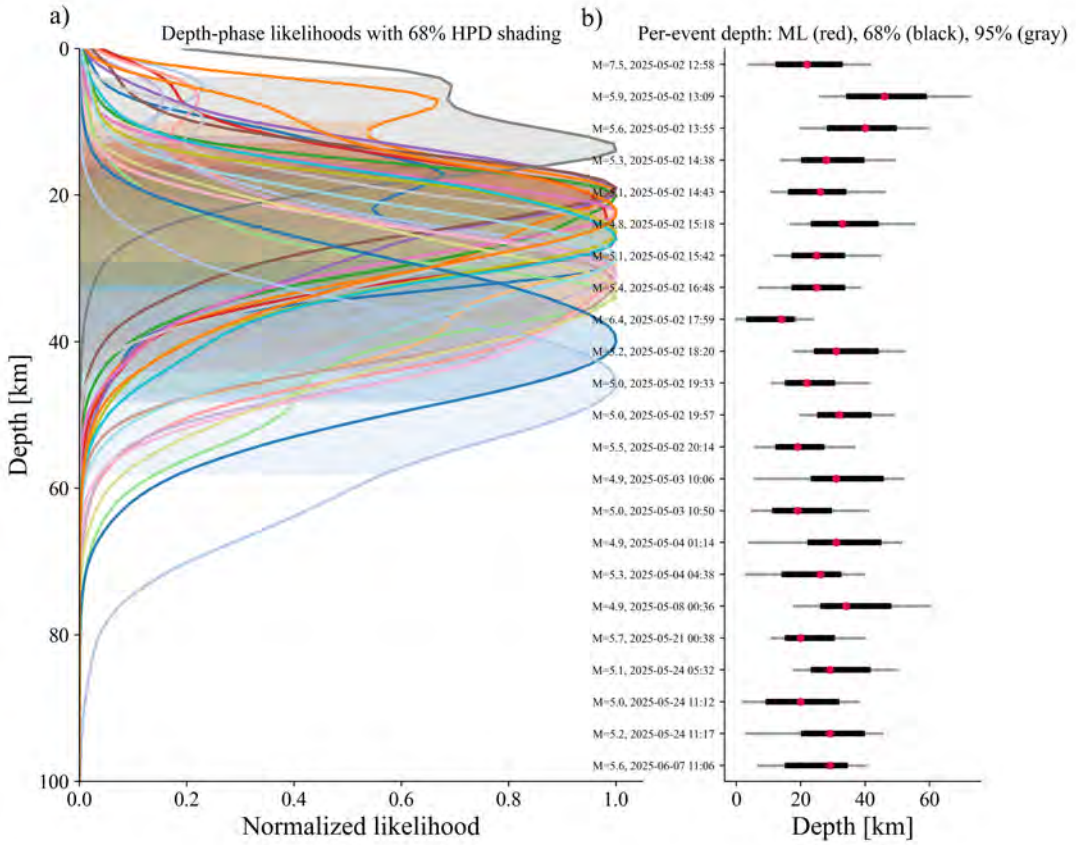


Figure 3. a) Normalized depth–phase likelihood functions for all analyzed events (left), computed from waveform-based depth-phase modeling using pP–P, sP–P, and related teleseismic depth-sensitive arrivals. For each event, the likelihood curve is shown together with its 68% highest posterior density (HPD) credible region, obtained via marginalization over phase picks and modeling uncertainties. Shading indicates the depth intervals where the posterior probability exceeds the 68% HPD threshold. b) Per-event depth solutions, including the maximum-likelihood (ML) depth estimate (red marker), 68% posterior credible interval (black bars), and 95% credible interval (gray bars). Events are ordered by origin time, and their magnitudes and timestamps are annotated accordingly. The reviewed centroid depth of the Mw 7.4 mainshock reported by the USGS is consistent with our estimate.

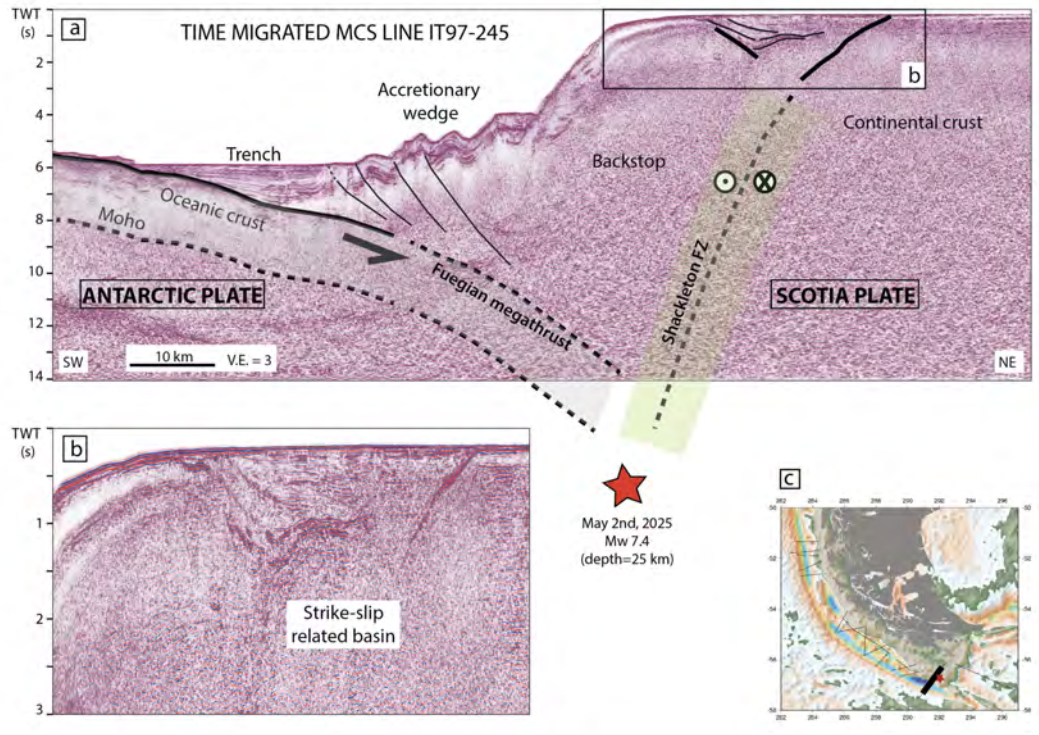


Figure 4. Seismic reflection profile IT97–245 crossing the southernmost Chilean margin, where the Chile Trench transitions into the Shackleton Fracture Zone (SFZ). (a) The profile illustrates the structural architecture of the plate boundary between the Antarctic and Scotia plates. The Fuegian megathrust (solid black line where imaged, dashed where interpreted) appears as a landward-dipping reflector beneath the accretionary wedge, marking the active subduction interface. Toward the northeast, a sedimentary basin develops where the SFZ impinges on the continental shelf, indicating significant deformation associated with the transform plate boundary system. The semi-vertical yellow zone marks the proposed deformation corridor of the Shackleton FZ, which accommodates oblique convergence and lateral displacement between plates. The transparent yellow area highlights the broader SFZ-related deformation zone, suggesting strain partitioning between thrust and strike-slip components consistent with oblique plate motion. The red star indicates the nucleation point of the May 2, 2025 mainshock (depth $\approx$ 25 km). (b) Zoomed view of the strike-slip–related basin, showing steeply dipping fault blocks and internal reflectors interpreted as syn-tectonic deposits formed under transtensional conditions during oblique plate motion. (c) Location map of seismic line IT97–245. The bold black line shows the segment of the profile interpreted in this work; thin black lines represent the dataset acquired in 1997 in Southern Chile and Antarctic. The uninterpreted seismic line is shown in Supplementary Figure S3.

Supporting Information for "The 2 May 2025 Mw 7.4 Drake Passage Earthquake: Insights into Tectonics at the Shackleton Fracture Zone–Chilean Trench intersection"

A. Vuan[1], G. Brancatelli[1], G. Brancolini[1], L. Gasperini[2], R. Geletti[1], E. Lodolo[1], A. Magrin[1], M. Menichetti[3], M. Plasencia[1], A. Polonia[2], M. Santulin[1], A. Tassone[4]

[1]Istituto Nazionale di Oceanografia e di Geofisica Sperimentale – OGS, Italy
[2]Istituto di Scienze Marine – CNR-ISMAR, Bologna, Italy
[3]Dipartimento di Scienze Pure ed Applicate, Università di Urbino, Urbino, Italy
[4]Instituto de Geociencias Básicas, Aplicadas y Ambientales de Buenos Aires (IGeBA), CONICET – Universidad de Buenos Aires, Argentina

Contents of this file

1. Text S1 to S5
2. Tables S1 to S5
3. Figures S1 to S8

S1 Relocation of the seismic events

The events of the 2 May 2025 seismic sequence were initially detected and located using our server, which monitors the area covered by the Antarctic Seismographic Argentinean Italian Network (ASAIN) in and around the Scotia Sea and the Antarctic Peninsula. In addition to data from our network, the SeisComP server (Helmholtz-Centre Potsdam–GFZ and Gempa, 2008) was configured to continuously receive data from approximately other 60 stations selected to detect events in the region (Table S1). Data from global networks were collected via international agencies and standard protocols. Between 2 May and 7 July 2025, the automatic monitoring system located 49 events following the Mw 7.4 mainshock in the Drake Passage, with magnitudes ranging between 4.0 and 6.4.

We manually reviewed the locations of the main events using only stations at regional distances ($< 28°$). We also relocated an additional event from March 27, 2007 (M 4.8), whose epicenter lies close to the 2025 sequence. The list of stations used in the relocation process is provided in Table S2, and Figure S1 shows their distribution together with the location of the mainshock. The two stations closest to the 2 May 2025 event are C1.MG01 (207 km) and AI.DSPA (316 km), both located in Tierra del Fuego. Other stations in southernmost South America lie up to ∼600 km away.

To achieve acceptable azimuthal coverage (azimuthal gap $< 180°$), we also included stations on the Antarctic Peninsula, in the Scotia Sea region, and in the nearest part of the polar plateau. Stations on the Antarctic Peninsula record fewer clear P phases than those in the polar region (with the exception of IU.PMSA), owing to high ambient noise levels (e.g., Vuan et al. (2000)). We selected P phases—and, for the closest stations, also S phases—and relocated the events using the LocSAT algorithm (Bratt & Nagy, 1991) together with the IASPEI91 velocity model (Kennett & Engdahl, 1991). When possible, event depths were left unfixed.

S2 Depth from pP and pS phases through machine learning models

The determination of earthquake depth using pP and sP phases involves analyzing the time difference between the arrival of these surface-reflected phases and the direct P wave. SeisBench, a framework for machine learning in seismology (Woollam et

al., 2022), facilitates this task by providing tools for robust identification of depth phases. The SeisBench interfaces *DepthPhaseTEAM* and *DepthPhaseNet* (Münchmeyer et al., 2023) allow users to input preliminary earthquake locations together with waveform data to estimate depth from the predicted arrival times of the pP and sP phases. DepthPhaseTEAM employs a multi-station probabilistic approach to determine event depth and quantify the associated uncertainties.

The workflow can be summarized as follows: (a) select high-quality stations at teleseismic distances; (b) predict approximate P-wave arrival times using global traveltime models; (c) download waveform data around these preliminary arrivals; (d) refine the P-wave picks using deep-learning–based predictions; and (e) estimate event depth using the IASPEI91 global velocity model and the time difference between the pP, sP, and direct P phases. This method is global in scope and does not account for potential biases in depth estimation caused by (1) local bathymetry or topography, (2) waveguides within the subducting plate that may introduce azimuthal variations, or (3) local shallow velocity structure (Münchmeyer et al., 2023).

The seismic data used in this analysis are freely available from the FDSN (Federation of Digital Seismological Networks; `https://www.fdsn.org/`), while preliminary earthquake locations were obtained from the GEOFON web services (`https://geofon.gfz.de/`). We used all available seismic stations located between 15° and 80° epicentral distance to evaluate potential pP and sP phases (Fig. S2). An initial station selection was performed by assessing the signal-to-noise ratio of the P-wave arrivals.

S3 Multichannel seismic reflection data and focal solutions

Multichannel seismic reflection profile IT97–245 was acquired off Tierra del Fuego by the Italian R/V *OGS-Explora* during the 1997 expedition, as part of the Italian Antarctic Research Program (Polonia et al., 2007). The multichannel seismic data were recorded using a 3000 m long SERCEL-357 streamer with 120 active channels and a 50 m shot interval, providing a nominal fold of 30 and a sampling interval of 2 ms. The source consisted of a 36-gun array with a total volume of 80 L.

A broadband processing sequence was applied at the OGS computing center to improve the signal-to-noise ratio by attenuating both coherent and incoherent noise (Fig. S3). The processing workflow included denoising, deghosting, multiple attenuation, amplitude recovery and balancing, multichannel predictive deconvolution, iterative velocity analysis, pre-stack time migration, and final post-stack time-variant filtering (Brancatelli et al., 2022).

Focal solutions discussed later in the text are retrieved from the Global CMT catalog (Dziewonski et al., 1981; Ekström et al., 2012) and compared with focal mechanisms determined from regional data and other agencies. Given the scarcity of nearby seismic stations, we rely primarily on globally available sources for focal mechanism information, including the Global Centroid Moment Tensor (GCMT) catalog from Harvard, USGS, Geoscience Australia, and GFZ (Table S3). These agencies use different global datasets and apply different inversion procedures. The principal differences between the Harvard/GCMT and the USGS solutions for large earthquakes (Mw $>$ 7) arise from their inversion methodologies: the GCMT approach relies on centroid moment tensor inversion using long-period surface waves and body waves, resolving the centroid location, which may differ significantly from the hypocenter; whereas the USGS typically employs a W-phase inversion for rapid, robust solutions, and may later provide additional products such as finite-fault models or multiple moment-tensor solutions (e.g., GCMT-style inversions or full-waveform approaches). Despite these methodological differences, both the GCMT and USGS place the 2025 mainshock at depths of 20 km or greater, which likely explains why no significant tsunami amplitudes were recorded.

S4 Tables

The following tables summarize the seismic and station datasets used in this study. Table S1 lists all seismic stations configured in the SeisComP monitoring system for automatic detection and location of regional earthquakes. Table S2 provides detailed station parameters and statistics of P- and S-phase arrivals used in the relocation procedure. Table S3 reports the focal mechanism solutions for the May 2, 2025 mainshock obtained from global agencies. Table S4 compiles GCMT fault-plane solutions since 1976 in the study area, highlighting the predominance of steeply dipping mechanisms. Table S5 includes GCMT mechanisms for earlier aftershocks of the 2025 sequence. Together, these tables document the observational foundation for the seismic analysis presented in the main text.

Table S1. Stations used by SeisComp server for automatic detection and location.

Network	**Stations**
AI	BELA, DSPA, JUBA, MBIO, ORCD, PTRA, SMAI
AU	MAW
AW	VNA1, VNA2, VNA3
C	GO04, GO06, GO08, GO10
C1	AC04, AY02, AY03, AY04, AY05, BI02, BO04, CO01, CO02, IN44, LL01, LL02, LL03, LL04, LL05, LL06, LR05, MG01, MG02, MG03, MG04, MG05, MT09
G	CCD, COYC, DRV, TRIS
GE	SNAA
GT	BOSA, CPUP, LBTB, LPAZ, PLCA, VNDA
II	EFI, HOPE, RPN
IU	LCO, PMSA, QSPA

Table S2. Station parameters used in the SeisComp location procedure.

net	sta	lon	lat	neve	np	ns	res_p	rms_p	D (deg)	azim
AI	BELA	-34.63	-77.88	9	9	0	-0.0	0.4	23.6	163.3
AI	DSPA	-68.27	-53.95	20	11	9	-0.0	1.3	3.2	352.8
AI	JUBA	-58.66	-62.24	2	2	0	-0.8	1.2	6.9	142.2
AI	MBIO	-56.62	-64.24	2	2	0	-0.1	1.0	9.2	147.9
AI	ORCD	-44.74	-60.74	3	3	0	-0.1	0.6	12.4	117.0
AI	PTRA	-56.23	-63.48	1	1	0	0.2	0.0	8.5	142.3
AI	SMAI	-67.11	-68.13	3	3	0	0.3	0.7	11.1	179.2
AW	VNA1	-8.28	-70.69	3	3	0	0.1	0.4	27.8	142.3
AW	VNA2	-7.39	-70.92	6	6	0	-0.4	0.4	28.1	142.9
AW	VNA3	-9.67	-71.24	6	6	0	-0.3	0.4	27.4	143.5
C	GO06	-71.47	-39.58	5	5	0	1.0	0.5	17.8	350.4
C	GO08	-72.56	-48.46	7	7	0	1.2	1.9	9.2	339.1
C	GO10	-71.05	-53.15	7	7	0	-0.5	0.9	4.5	331.5
C1	AC04	-71.07	-28.20	6	6	0	-0.4	0.4	29.1	353.6
C1	AY02	-73.19	-46.48	2	2	0	1.7	0.6	11.1	339.4
C1	AY03	-72.59	-47.25	4	4	0	1.4	0.4	10.4	340.4
C1	AY04	-71.69	-46.58	1	1	0	1.1	0.0	11.1	343.5
C1	AY05	-73.51	-45.15	5	5	0	0.6	1.6	12.6	340.1
C1	BI02	-71.27	-36.66	8	8	0	0.2	0.6	20.7	351.6
C1	BO04	-70.61	-33.99	1	1	0	-0.4	0.0	23.1	353.6
C1	CO01	-70.09	-29.98	8	8	0	0.5	0.5	27.3	355.3
C1	CO02	-71.00	-31.20	7	7	0	-0.2	0.5	26.1	353.2
C1	IN44	-59.66	-62.48	2	2	0	-0.3	0.7	6.8	147.2
C1	LL01	-72.41	-42.38	5	5	0	1.9	1.7	15.2	345.9
C1	LL02	-71.85	-43.19	8	8	0	1.5	1.7	14.2	347.5
C1	LL03	-72.40	-41.14	4	4	0	0.6	0.2	16.4	346.5
C1	LL04	-72.41	-40.91	4	4	0	0.7	0.2	16.6	346.8
C1	LL05	-73.47	-41.41	6	6	0	1.3	0.9	16.2	343.7
C1	LR05	-72.00	-40.23	7	7	0	1.1	0.7	17.2	348.4
C1	MG01	-67.63	-54.93	19	11	8	-1.6	0.7	2.2	359.9
C1	MG02	-69.22	-52.78	12	10	2	-0.9	0.6	4.5	347.4
C1	MG03	-70.46	-53.85	18	10	8	-1.0	0.6	3.7	332.7
C1	MG04	-71.57	-52.86	11	8	3	-1.5	0.8	4.8	330.7
C1	MG05	-72.50	-51.68	1	1	0	-2.9	0.0	5.8	334.7
C1	MT09	-70.99	-33.78	7	7	0	-1.0	0.2	23.6	352.7
GE	SNAA	-2.84	-71.67	7	7	0	-0.7	0.6	29.7	144.6
GT	CPUP	-57.33	-26.33	2	2	0	-2.1	0.6	31.7	17.4
GT	LPAZ	-68.13	-16.29	3	3	0	0.1	0.5	40.7	358.8
GT	PLCA	-70.55	-40.73	9	9	0	1.3	1.5	16.6	352.0
GT	VNDA	161.85	-77.52	1	1	0	1.0	0.0	42.3	194.2
II	EFI	-58.06	-51.68	2	1	1	-0.3	0.0	7.5	47.8
II	HOPE	-36.49	-54.28	8	8	0	0.7	0.3	17.6	93.7
IU	LCO	-70.70	-29.01	6	6	0	-0.1	0.6	28.3	354.1
IU	PMSA	-64.05	-64.77	11	11	0	-0.0	0.6	7.9	169.0
IU	QSPA	144.44	-89.93	1	1	0	1.0	0.0	33.2	180.1
IU	TRQA	-61.98	-38.06	1	1	0	0.1	0.0	19.3	12.1

Table S3. Focal solutions available for the mainshock – GCMT = Global Centroid Moment Tensor Harvard, USGS = United States Geological Survey, GAUS = Geoscience Australia, GFZ = Helmholtz Centre for Geosciences.

Agency	Strike1	Dip1	Rake1	Strike2	Dip2	Rake2	Mw	Depth (km)
GCMT	326	38	99	134	52	83	**7.4**	**20**
USGS	310	33	93	128	57	88	**7.4**	**23.5**
GAUS	348	45	134	115	59	56	**7.5**	**12**
GFZ	152	60	93	326	30	84	**7.45**	**10**

Table S4. Fault plane solutions from GCMT since 1976 in the area. Close to the mainshock of May 2, 2025, the dip angles are greater than 34°. Some mechanisms at higher dip are strike slip events.

Lon	Lat	Strike	Dip	Rake	Strike1	Dip1	Rake1	Man	Exp	Datetime
-66.69	-57.42	300	41	57	160	57	115	1.350	24	1980050200
-65.02	-58.30	294	66	-8	27	83	-156	1.410	24	1984040500
-66.90	-57.56	167	90	180	257	90	0	1.690	24	1987062100
-66.38	-57.22	189	79	169	281	79	11	6.500	23	1991060300
-66.42	-57.67	115	45	56	339	54	119	7.690	24	1995030100
-66.16	-57.94	112	70	16	16	75	159	2.887	25	2010011712
-66.33	-57.75	334	44	97	144	46	83	5.593	23	2010012019
-65.76	-57.59	201	82	179	291	89	8	2.833	25	2012041410
-66.85	-57.74	130	49	-1	220	89	-139	5.132	23	2015031400
-65.99	-57.48	208	79	-169	115	79	-12	2.376	24	2015102020
-66.75	-57.42	341	38	99	149	53	83	3.436	23	2016031003
-68.98	-56.78	27	72	167	121	78	19	2.805	23	2016071121
-69.11	-56.74	34	74	173	126	83	17	3.191	23	2016071121
-66.60	-57.55	140	42	67	349	52	109	3.874	25	2018102906
-66.43	-57.69	121	46	48	353	58	125	6.678	24	2018102920
-66.55	-57.66	130	38	48	359	63	118	3.461	24	2018102921
-66.49	-57.40	171	38	107	329	54	77	3.872	23	2018103112
-66.22	-57.48	334	46	75	176	46	105	3.409	23	2018110816
-66.41	-57.59	170	43	112	321	51	71	6.495	23	2018111607
-66.32	-57.79	108	54	35	355	63	138	8.307	23	2019090516
-67.79	-57.17	323	34	85	149	57	93	3.702	23	2019122120

Table S5. GCMT focal mechanisms for earlier aftershocks of the May 2, 2025, event.

Lon	Lat	Strike	Dip	Rake	Strike1	Dip1	Rake1	Mantissa	Exp	Datetime
-67.22	-57.38	326	37	105	128	55	79	4.264	25	2025050217
-67.21	-57.15	23	61	176	115	86	29	6.715	23	2025052100
-67.06	-57.43	304	43	74	145	49	104	1.059	24	2025060711
-67.24	-57.18	22	72	-170	289	81	-18	3.009	24	2025070415

S5 Figures

The following figures illustrate the datasets, analytical steps, and structural interpretations supporting the results presented in this study. Figure S1 shows the distribution of stations used for manual revision of the seismic sequence, while Figure S2 displays the hypocentral location of the May 2, 2025 mainshock together with the stations employed for depth-phase evaluation. Figure S3 presents the uninterpreted multichannel seismic profile IT97–245, and Figure S4 summarizes station residuals used during event relocation. Figure S5 illustrates epicentral uncertainty ellipses for the revised events. Figure S6 provides the sensitivity analysis of depth estimates based on pP–P delays, and Figure S7 shows rose diagrams of P- and T-axis azimuths derived from focal mechanisms. Finally, Figure S8 depicts the temporal and spatial variation of dip angles within the study area. Together, these figures document the seismological and structural constraints underpinning the interpretation of the 2025 seismic sequence.

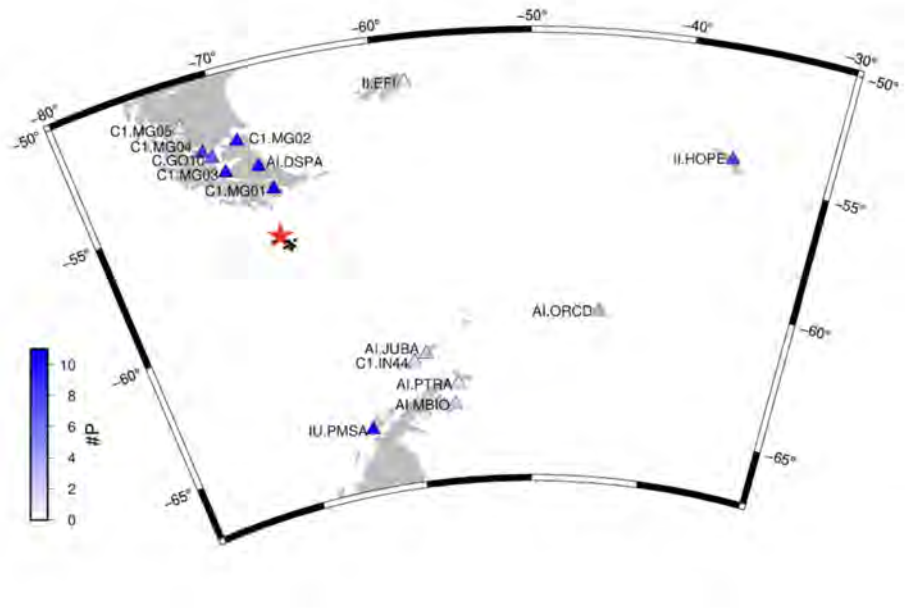


Figure S1. Stations used for manual revision; the color indicates the number of P-phases used for each station.

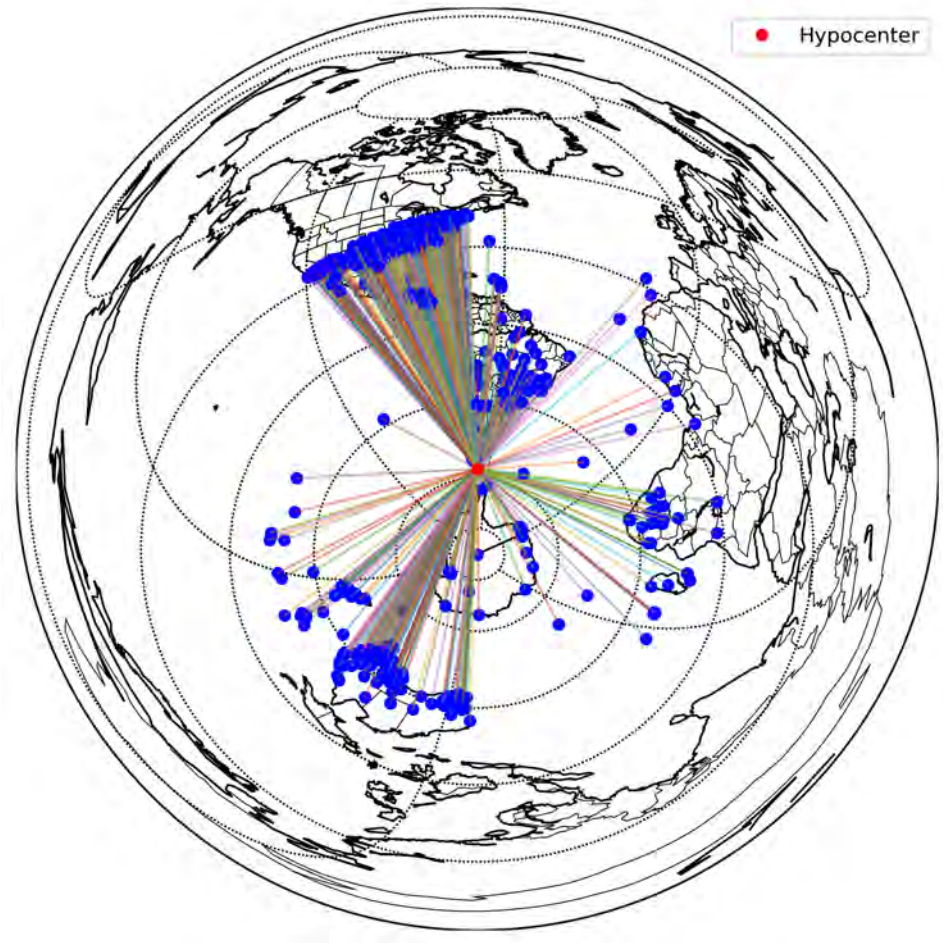


Figure S2. Hypocenter location of the May 2, 2025 mainshock and stations (blue dots) used to evaluate pP - P based depth.

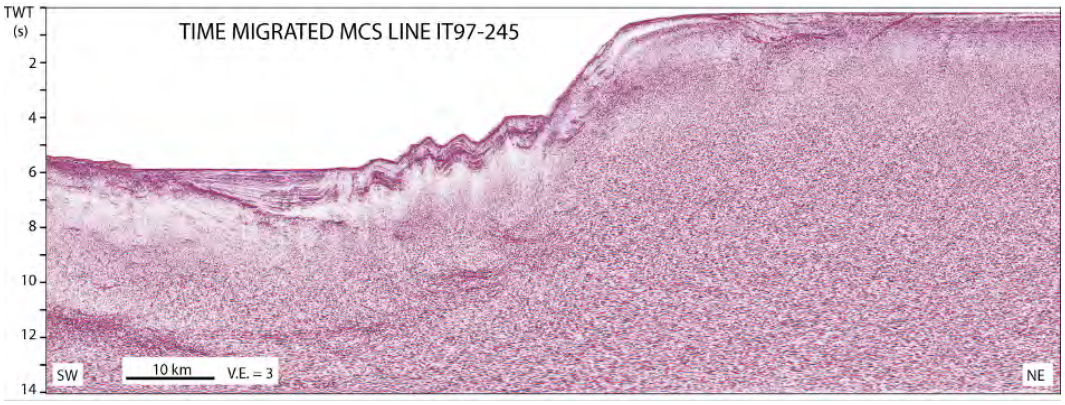


Figure S3. Uninterpreted multichannel seismic line IT97-245 described in this work.

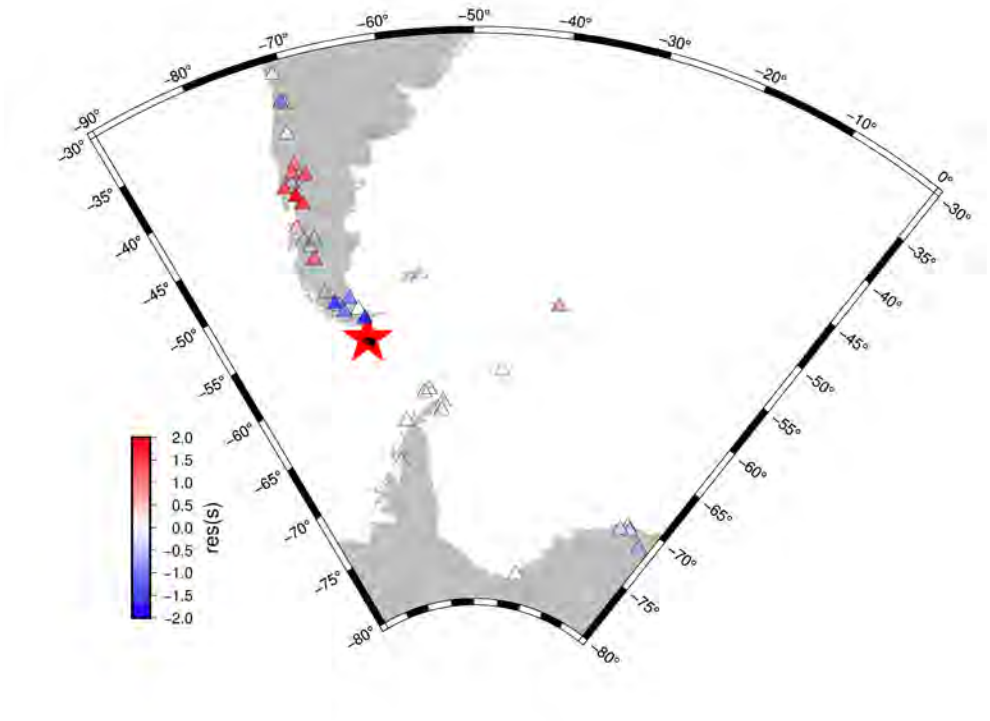


Figure S4. Stations used for the relocation of events. The color scale shows the average residual for each station when more than 5 P-phases are available.

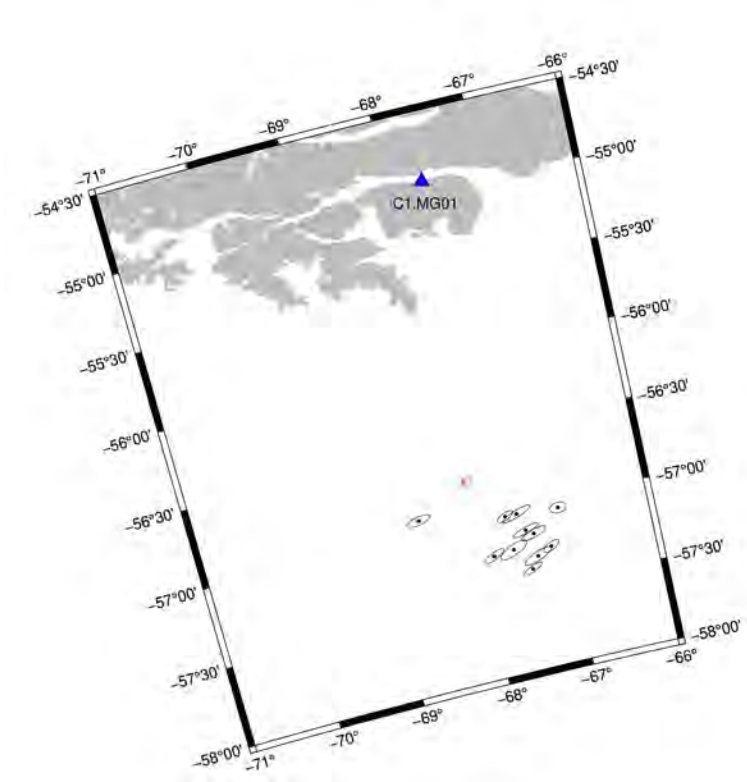


Figure S5. Uncertainty ellipses of the epicenters for the revised events. Location of the mainshock and uncertainty ellipse in red.

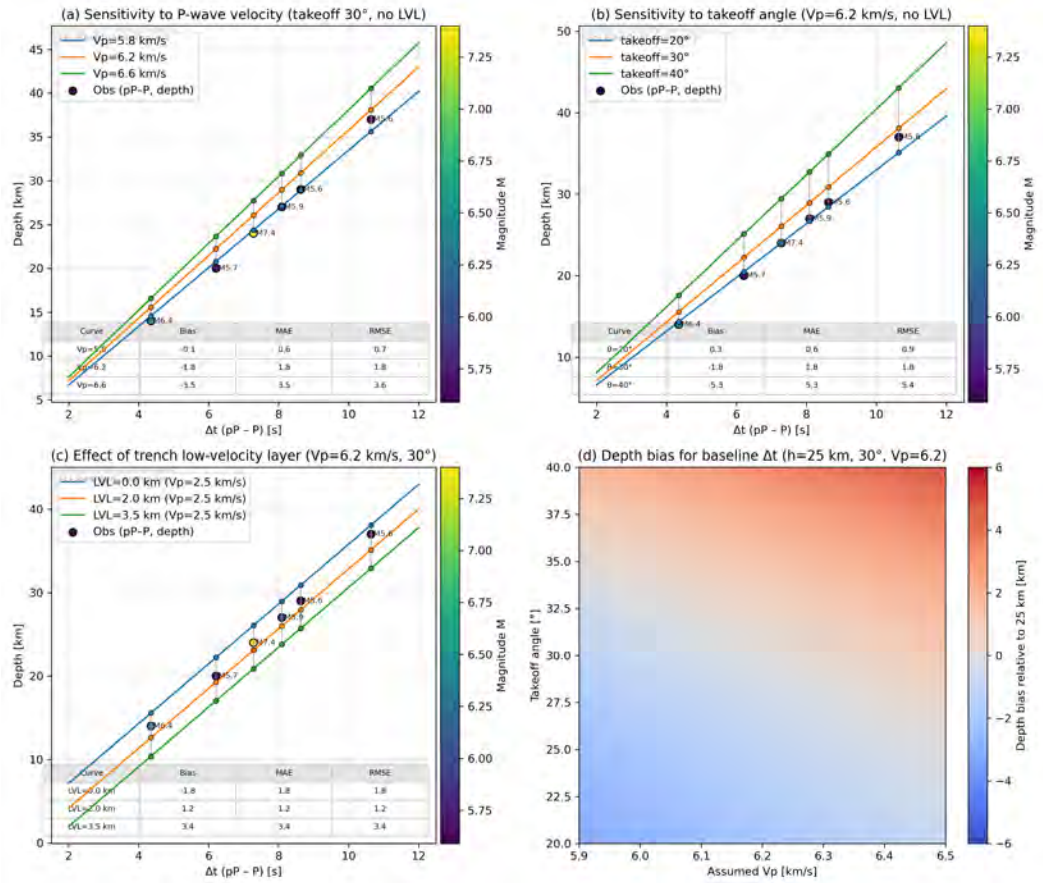


Figure S6. Sensitivity of pP–P–inferred depths with panel-wise residuals. (a) Depth inferred from the pP–P delay Δt for different crustal P-wave velocities V_p (takeoff angle 30°; no low-velocity layer, LVL). (b) Depth versus Δt for different takeoff angles θ ($V_p = 6.2$ km/s; no LVL). (c) Depth versus Δt for different LVL thicknesses. Observed events are plotted as circles at (Δt, estimated depth). For each observation, a thin vertical line at the measured Δt carries colored markers indicating the depths predicted by each sensitivity curve in the panel. The on-panel summary tables report the bias, mean absolute error (MAE), and root mean square error (RMSE), all in km, of the residuals defined as $\text{Depth}_{\text{obs}} - \text{Depth}_{\text{inf}}(\Delta t;$ panel parameters), where positive residuals imply underestimation by the model. (d) Heat map of depth bias (for an inferred depth of 25 km) as a function of assumed V_p and θ.

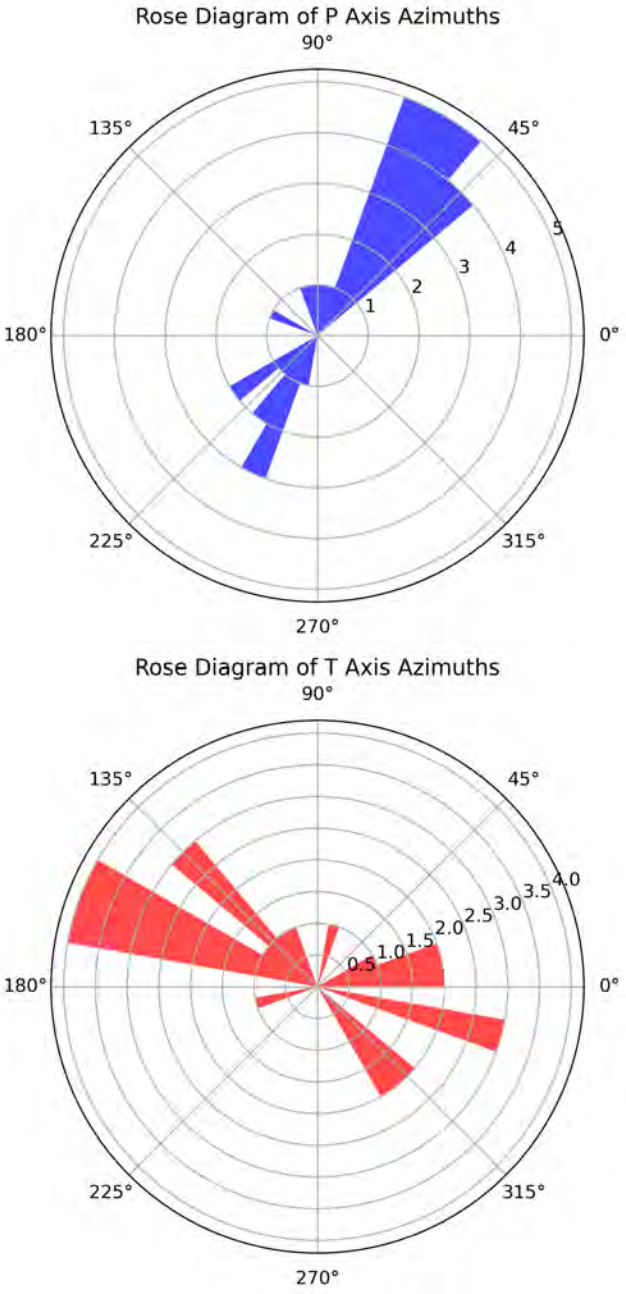


Figure S7. Rose diagrams showing the directional distribution of P- and T-axis azimuths derived from focal mechanism solutions. The top panel illustrates the frequency of P-axis orientations, while the bottom panel shows T-axis orientations. Each bar represents the number of events with azimuths falling within 10° directional bins, highlighting dominant stress orientations in the region.

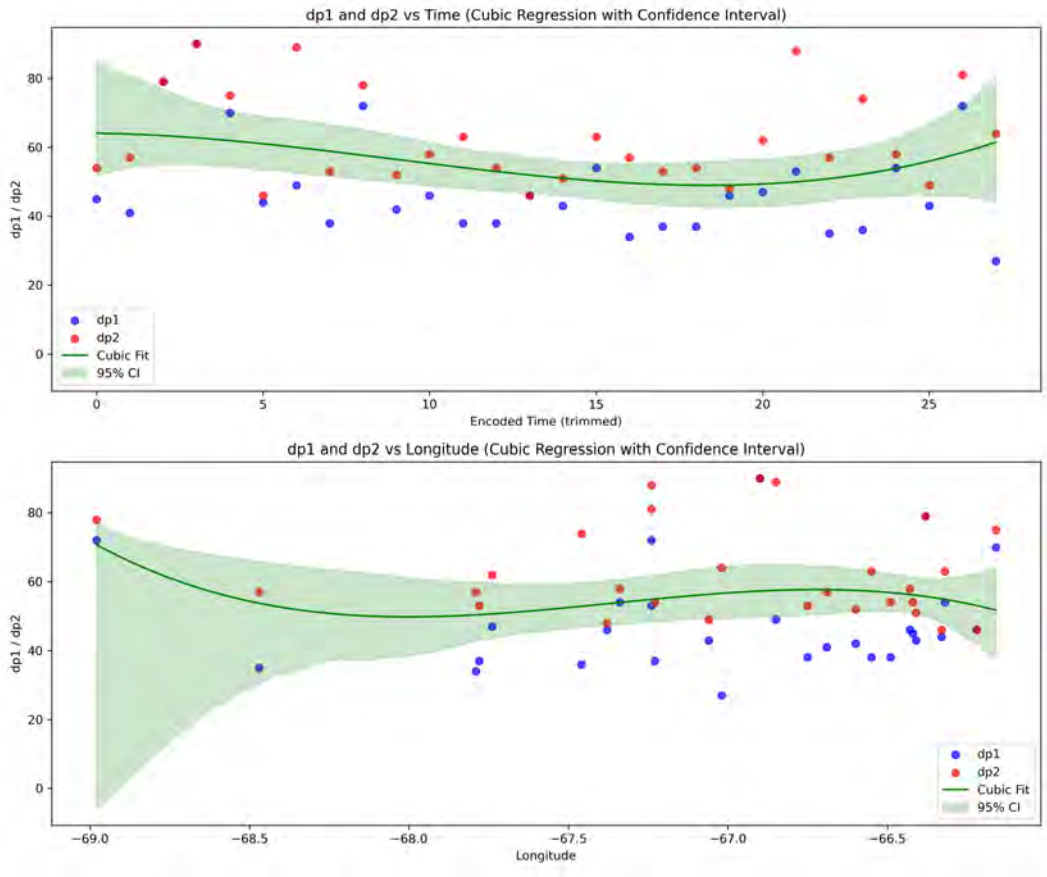


Figure S8. (top) Temporal and (bottom) spatial variation of dip angles from collected focal mechanisms in the study area. The plot illustrates changes in fault-plane dip angles as a function of event time and longitude, providing insights into the evolution of rupture geometry and deformation style during the seismic sequence. Variations in dip may reflect differences in fault orientation, stress regime, and structural segmentation along the plate boundary.

References

Brancatelli, G., Forlin, E., Bertone, N., Del Ben, A., & Geletti, R. (2022). Chapter 7 - time to depth seismic reprocessing of vintage data: A case study in the Otranto Channel (South Adriatic Sea). In R. Bell, D. Iacopini, & M. Vardy (Eds.), *Interpreting subsurface seismic data* (p. 157-197). Elsevier. doi: 10.1016/B978-0-12-818562-9.00009-1

Bratt, S. R., & Nagy, W. (1991). *The LocSAT Program* (Tech. Rep.). San Diego, CA: Science Applications International Corporation (SAIC). (User manual/report)

Dziewonski, A. M., Chou, T.-A., & Woodhouse, J. H. (1981). Determination of earthquake source parameters from waveform data for studies of global and regional seismicity. *Journal of Geophysical Research: Solid Earth*, *86*(B4), 2825–2852. doi: 10.1029/JB086iB04p02825

Ekström, G., Nettles, M., & Dziewonski, A. M. (2012). The global CMT project 2004–2010: Centroid-moment tensors for 13,017 earthquakes. *Physics of the Earth and Planetary Interiors*, *200–201*, 1–9. doi: 10.1016/j.pepi.2012.04.002

Kennett, B. L. N., & Engdahl, E. R. (1991). Traveltimes for global earthquake location and phase identification. *Geophysical Journal International*, *105*(2), 429–465. doi: 10.1111/j.1365-246X.1991.tb06724.x

Münchmeyer, J., Saul, J., & Tilmann, F. (2023). Learning the Deep and the Shallow: Deep-Learning-Based Depth Phase Picking and Earthquake Depth Estimation. *Seismological Research Letters*, *95*(3), 1543–1557. doi: 10.1785/0220230187

Polonia, A., Torelli, L., Brancolini, G., & Loreto, M.-F. (2007). Tectonic accretion versus erosion along the southern Chile trench: Oblique subduction and margin segmentation. *Tectonics*, *26*, TC3005. doi: 10.1029/2006TC001983

Vuan, A., Russi, M., & Panza, G. (2000). Group Velocity Tomography in the Subantarctic Scotia Sea Region. *Pure and Applied Geophysics*, *157*, 1337–1357. doi: 10.1007/PL00001122

Woollam, J., Münchmeyer, J., Tilmann, F., Rietbrock, A., Lange, D., Bornstein, T., ... Soto, H. (2022). SeisBench—A Toolbox for Machine Learning in Seismology. *Seismological Research Letters*, *93*(3), 1695–1709. doi: 10.1785/0220210324